High-resolution spectroscopy and analysis of the $\nu 3$, $\nu 4$ and $2\nu 4$ bands of SiF4 in natural isotopic abundance

V. Boudon, L. Manceron, Cyril Richard

▶ **To cite this version:**

V. Boudon, L. Manceron, Cyril Richard. High-resolution spectroscopy and analysis of the $\nu 3$, $\nu 4$ and $2\nu 4$ bands of SiF4 in natural isotopic abundance. Journal of Quantitative Spectroscopy and Radiative Transfer, 2020, 253, pp.107114. 10.1016/j.jqsrt.2020.107114 . hal-03027596

HAL Id: hal-03027596
https://hal.science/hal-03027596

Submitted on 27 Nov 2020

HAL is a multi-disciplinary open access archive for the deposit and dissemination of scientific research documents, whether they are published or not. The documents may come from teaching and research institutions in France or abroad, or from public or private research centers.

L'archive ouverte pluridisciplinaire **HAL**, est destinée au dépôt et à la diffusion de documents scientifiques de niveau recherche, publiés ou non, émanant des établissements d'enseignement et de recherche français ou étrangers, des laboratoires publics ou privés.

High-resolution spectroscopy and analysis of the ν_3, ν_4 and $2\nu_4$ bands of SiF_4 in natural isotopic abundance

V. Boudon[a,*], L. Manceron[b,c], C. Richard[a]

[a] *Laboratoire Interdisciplinaire Carnot de Bourgogne, UMR 6303 CNRS - Université Bourgogne Franche-Comté, 9 avenue Alain Savary, BP 47870, F-21078 Dijon Cedex, France*
[b] *Synchrotron SOLEIL, AILES Beamline, L'Orme des Merisiers, BP48, F-91192 St-Aubin Cedex, France*
[c] *MONARIS, UMR 8233, Université Pierre et Marie Curie, 4 Place Jussieu, case 49, F-75252 Paris Cedex 05, France*

Abstract

Silicon tetrafluoride (SiF_4) is a trace component of volcanic gases. However, a better knowledge of spectroscopic parameters is needed for this molecule in order to derive accurate concentrations. This motivated FTIR measurements with high-spectral resolution (0.001 cm^{-1}) and an extensive study of its infrared absorption bands, including the fundamentals and overtone and combinations. We present here a detailed analysis and modeling of the strongly absorbing ν_3 and ν_4 fundamental bands, for the three isotopologues in natural abundance: $^{28}SiF_4$ (92.23 %), $^{29}SiF_4$ (4.67 %) and $^{30}SiF_4$ (3.10 %). It includes a global fit with consistent parameter sets for the ground and excited states. In particular, all existing rotational line data have been included. The $2\nu_4$ band of $^{28}SiF_4$ could also be analyzed in detail. A first fit of the dipole moment derivative for the ν_3 band for $^{28}SiF_4$ has been performed, along with two independent estimates of the integrated band intensity; the results are consistent with literature values, around 690 km/mol. The isotopic dependence of band centers and Coriolis parameters has also been studied. TFSiCaSDa, a new database of cross sections and calculated lines for the ν_3 band of SiF_4, has been set up.

Keywords:
Sulfur tetrafluoride, High-resolution infrared spectroscopy, Line positions, Line intensities, Tensorial formalism, Isotopologues, Molecular spectroscopy database

1. Introduction

Volcanoes reject large amounts of sulfur-containing gases in the atmosphere; these represent 10 to 15 % of the anthropogenic sulfur emissions. Tetrafluorosilane, or silicon tetrafluoride (SiF_4) is a trace component of fumarole gases on volcanoes, arising from interactions between magmatic HF and wall rocks [1] and lends itself well to remote open-path IR spectroscopic detection with a strong absorption band at 1032 cm^{-1} (the ν_3 stretching fundamental

*Corresponding author (phone: +33.3.80.39.59.17, fax: +33.3.80.39.59.71)
Email address: vincent.boudon@u-bourgogne.fr (V. Boudon)

band). However, the volcanological literature on SiF_4 is minimal compared to other gases. Some studies report that the possible importance of SiF_4 had been neglected because of the problems of reporting HF and SiF_4 separately in conventional analyses [1]. FTIR measurements have been used to infer volcanic plume composition, including SiF_4. For instance, it has been identified among other species in the volcanic plumes of Etna [1, 2], Popocatépetl [3, 4, 5, 6] or Satsuma-Iwojima [7] volcanoes through remote-sensing FTIR spectroscopy. In particular, the SiF_4/SO_2 ratio has been proposed as a marker of deep magma increased pressure in volcano magmatic chambers and domes [1, 8]. It has even been suggested that silicon tetrafluoride should be present on Io, the highly volcanic moon of Jupiter [9]. A correct and quantitative detection thus requires a good knowledge of the molecule's infrared spectrum, both in terms of line positions and line intensities.

SiF_4 spectroscopy is not, at present, very well known. After some earlier works concerning force constants [10] and band contours [11, 12], there exist some pioneering high-resolution studies of the ν_3 fundamental [13, 14, 15] and of the $3\nu_3$ overtone [16] bands, along with some global estimates of integrated band intensities [17]. Some ν_3 lines were measured at ultra-high resolution for metrology purposes [18]. Overtone and combination vibrational levels have been investigated theoretically [19]. The ν_3 dipole moment derivative has been estimated using a few isolated lines [13]. The ground state has also been investigated with a few rotational lines recorded in the microwave region [20] and also using sideband lasers [21, 22]. The Stark effect was investigated in the ground state [23] and in the ν_3 band [24]. All these studies, however, are rather incomplete and do not allow full band modeling. Moreover, they only concern cold bands for room-temperature modeling for the main isotopologue ($^{28}SiF_4$).

We thus present here a detailed investigation of the infrared absorption spectroscopy of SiF_4, based on new high-resolution spectra of several bands that allowed us to fit effective Hamiltonian parameters for the ground, $v_3 = 1$, $v_4 = 1$ and $v_4 = 2$ states. The ν_3 and ν_4 fundamental bands could be analyzed for the three isotopologues that are present in natural abundance: $^{28}SiF_4$ (92.23 %), $^{29}SiF_4$ (4.67 %) and $^{30}SiF_4$ (3.10 %). We could also perform very first fit of the ν_3 dipole moment derivative as well as two distinct estimates of the integrated band intensity for $^{28}SiF_4$, that compare quite well with literature values. Sections 2 and 3 present the experimental and theoretical details, respectively. Then, in Section 4, we present and discuss the results of the analyses. We include a study of the isotopic dependence of band centers and Coriolis parameters for the ν_3 and ν_4 fundamental bands, following our recent theoretical study on this topic [25].

2. Experimental details

High resolution spectra of pure SiF_4 and SiF_4/N_2 diluted mixtures were recorded on the AILES beamline at Synchrotron SOLEIL (Saint-Aubin, France) using a IFS125 Bruker interferometer (Maximum Optical Path Difference - MOPD = 882 cm) and a 51 mm path, stainless steel, coolable cell equipped with diamond windows, which has been described already [26]. The cell temperature was continuously monitored and the pressure was measured using a thermostated MKS capacitive gauge located about 300 mm away from the

measurement cell. As both the cell and the pressure gauge had comparable volumes, thermomolecular effects affected notably the low pressure measurements at low temperature. To alleviate this difficulty, a highly diluted, 4.6 % SiF_4/N_2 mixture was first prepared in a 3 l volume and allowed to mix for an hour. Next, about 3.6 mb of the mixture, more precisely measurable, were introduced in the cold cell. SiF_4 (Union Carbide, USA, 99 %) and Nitrogen gas (Air Liquide, France, 99.999 %) were used without further purification.

Table 1 gathers the experimental parameters which were adjusted for the twelve spectra used in this study. All mid IR spectra were recorded with a home-made high sensitivity HgCdTe with 4 K-cooled filters [27] and FIR spectra with a 4 K-cooled composite bolometer (IR lab, USA). The interferograms were transformed without apodization (boxcar option) and averaged. The spectral resolution (defined as 0.9/Optical Path Difference - OPD, in the Bruker instrument software) was varied from 0.00102 to 0.003 cm^{-1}, to maximize the data quality, depending on the sample pressure. The low pressure data were taken at the highest possible OPD here, while for some spectra of weak bands recorded at higher pressure, the spectral resolution was 0.0015 and 0.003 cm^{-1} to reduce spectral noise, but remained smaller than the effective linewidths. Transmission spectra were calculated with respect to an empty cell background taken at 0.02 cm^{-1} resolution. The wavenumber scales of the spectra were calibrated using OCS, CO_2 or H_2O lines [28] from a separate spectrum measured with the exact same set-up at the end of the series. In the mid infrared, 175 lines of OCS were used with a dispersion of 1.3×10^{-5} cm^{-1} (one sigma) after calibration with respect to the HITRAN 2016 values. In the far infrared, 47 lines of CO_2 and H_2O were used, with a dispersion of 7×10^{-5} cm^{-1} (one sigma) after calibration. Overall, frequency accuracy can thus be estimated to about 2×10^{-4} cm^{-1}.

[Table 1 here.]
[Figure 1 here.]

3. Theoretical model

SiF_4, just like CH_4, SiH_4 and other tetrahedral spherical top molecules with T_d point group symmetry at equilibrium, possesses four normal modes of vibration [19]: one non-degenerate mode with A_1 symmetry (ν_1, wavenumber $\sim$ 801 cm^{-1}), one doubly-degenerate mode with E symmetry (ν_2, wavenumber $\sim$ 264 cm^{-1}), and two triply-degenerate modes with F_2 symmetry (ν_3 and ν_4, wavenumber $\sim$ 1031.5 cm^{-1} and $\sim$ 388.4 cm^{-1}, respectively). Only F_2 fundamentals are infrared active, at first approximation.

3.1. Effective Hamiltonian

In this paper we use the theoretical model based on the tensorial formalism and the vibrational extrapolation concept developed by the Dijon group [29, 30, 31]. It takes full advantage of the molecule's high symmetry. Let us just recall briefly the principles of this model which have been already detailed in Ref. [31]. Considering an XY_4 molecule such as SiF_4, the vibrational levels can be grouped in series of polyads named P_k with $k = 0, \ldots, n$. For $k = 0$, we have P_0 which is the ground state (GS). The Hamiltonian operator is written

as follows (assuming that some perturbative treatment like a contact transformation [29] has been performed in order to eliminate inter-polyad interactions):

$$\mathcal{H} = \mathcal{H}_{\{P_0 \equiv GS\}} + \mathcal{H}_{\{P_1\}} + \ldots + \mathcal{H}_{\{P_k\}} + \ldots + \mathcal{H}_{\{P_{n-1}\}} + \mathcal{H}_{\{P_n\}}. \tag{1}$$

where the different $\mathcal{H}_{\{P_k\}}$ terms are expressed in the following form:

$$\mathcal{H}_{\{P_k\}} = \sum_{\text{all indexes}} t^{\Omega(K,n\Gamma)\Gamma_v\Gamma'_v}_{\{s\}\{s'\}} \beta \left[{}^{\varepsilon}V^{\Omega_v(\Gamma_v\Gamma'_v)\Gamma}_{\{s\}\{s'\}} \otimes R^{\Omega(K,n\Gamma)} \right]^{(A_1)}. \tag{2}$$

In this equation, the $t^{\Omega(K,n\Gamma)\Gamma v\Gamma' v}_{\{s\}\{s'\}}$ are the parameters to be determined by fitting assigned experimental line positions, while ${}^{\varepsilon}V^{\Omega_v(\Gamma_v\Gamma'_v)\Gamma}_{\{s\}\{s'\}}$ and $\mathrm{R}^{\Omega(K,n\Gamma)}$ are vibrational and rotational operators, respectively. For each term, Ω_v and Ω represent the degree in elementary vibrational operators (creation a^+ and annihilation a operators), and rotational operators (components J_x, J_y and J_z of the angular momentum), respectively. β is a factor that allows the scalar terms (terms with $\Gamma = A_1$, the totally symmetric irreducible representation of T_d) to match the "usual" contributions like $B_0 J^2$, *etc*. The order of each individual term is defined as $\Omega + \Omega_v - 2$. We deal with the effective Hamiltonians which are obtained, for a given polyad P_k, by the projection of H on the P_n Hilbert subspace:

$$\begin{aligned} \widetilde{H}^{<P_n>} &= P^{<P_n>}\mathcal{H}P^{<P_n>} \\ &= H^{<P_n>}_{\{\mathrm{GS}\}} + H^{<P_n>}_{\{P_1\}} + \ldots + H^{<P_n>}_{\{P_k\}} + \ldots + H^{<P_n>}_{\{P_{n-1}\}} + H^{<P_n>}_{\{P_n\}}. \end{aligned} \tag{3}$$

In the case of silicon tetrafluoride, for which there is no simple relation between the fundamental band wavenumbers (which are all quite well isolated), we use the following effective Hamiltonians:

- The ground state effective Hamiltonian,

$$\widetilde{H}^{<\mathrm{GS}>} = H^{<\mathrm{GS}>}_{\{\mathrm{GS}\}}. \tag{4}$$

- The ν_3 stretching fundamental effective Hamiltonian,

$$\widetilde{H}^{<\nu_3>} = H^{<\nu_3>}_{\{\mathrm{GS}\}} + H^{<\nu_3>}_{\{\nu_3\}}. \tag{5}$$

- The ν_4 bending fundamental effective Hamiltonian,

$$\widetilde{H}^{<\nu_4>} = H^{<\nu_4>}_{\{\mathrm{GS}\}} + H^{<\nu_4>}_{\{\nu_4\}}. \tag{6}$$

- The $2\nu_4$ bending overtone effective Hamiltonian,

$$\widetilde{H}^{<2\nu_4>} = H^{<2\nu_4>}_{\{\mathrm{GS}\}} + H^{<2\nu_4>}_{\{\nu_4\}} + H^{<2\nu_4>}_{\{2\nu_4\}}. \tag{7}$$

  In this case, the $v_4 = 2$ vibrational features three vibrational sublevels with respective symmetry A_1, E and F_2 since $[F_2 \otimes F_2] = A_1 + E + F_2$ ($[\ldots]$ representing the symmetric part of the direct product of the irreducible representation F_2 of the mode with itself). As a consequence, the $\widetilde{H}^{<2\nu_4>}_{\{2\nu_4\}}$ effective Hamiltonian contains three anharmonicity constants, as well as rovibrational operators corresponding to each of the three sublevels, but also to the interactions between them (see below).

3.2. Effective dipole moment

In order to calculate transition intensities, we also need to expand the effective dipole moment operator, in a very similar way to what we did recently in the case of the RuO_4 molecule [32]. This is again done using tensorial formalism, as described elsewhere [29, 30, 31]. In short, this operator, just as the effective Hamiltonian, is expanded as a sum of rovibrational operators [29]. In the case of the ν_3 stretching band, it appears here sufficient to expand it up to order one, which amounts to two operators and thus to two associated parameters to be fitted using experimental line intensities:

$$\widetilde{\mu}^{<\nu_3-GS>} = \mu^0_{\nu_3} {}^{+}V^{1(A_1F_2)F_2}_{\{GS\}\{\nu_3\}} + \mu^1_{\nu_3} \left(R^{1(1,0F_1)} \otimes {}^{-}V^{1(A_1F_2)F_2}_{\{GS\}\{\nu_3\}} \right)^{(F_2)}, \tag{8}$$

where we used a simplified notation for the effective parameters. Here, $\mu^0_{\nu_3}$ is the dipole moment derivative relative to the q_3 normal mode coordinates and $\mu^1_{\nu_3}$ is a rovibrational contribution that corresponds to the usual Herman–Wallis factor. In the above Equation, the R and V symbols represent rotational and vibrational operators, just as in the case of the effective Hamiltonian operator, as described above. This two-parameter model is used in Section 4.2 below to fit $\mu^0_{\nu_3}$ and $\mu^1_{\nu_3}$ using experimental line intensities for the $^{28}SiF_4$ isotopologue.

In the case of the ν_4 and $2\nu_4$ bands, we only consider here relative intensities. Thus, order 0 is sufficient and this leads in each case to a single parameter whose absolute value is not determined in the present study, so is is just fixed to 1.

$$\widetilde{\mu}^{<\nu_4-GS>} = \mu^0_{\nu_4} {}^{+}V^{1(A_1F_2)F_2}_{\{GS\}\{\nu_4\}}, \tag{9}$$

$$\widetilde{\mu}^{<2\nu_4-GS>} = \mu^0_{2\nu_4} {}^{+}V^{2(A_1F_2)F_2}_{\{GS\}\{2\nu_4\}}. \tag{10}$$

3.3. Basis sets and line intensities

The calculation of the effective Hamiltonian and effective dipole moment matrix elements are performed in the coupled rovibrational basis

$$\left| \left[\Psi^{(C_v)}_v \otimes \Psi^{(J,nC_r)}_r \right]^{(C)} \right\rangle, \tag{11}$$

where $\Psi^{(J,nC_r)}_r$ is a rotational wavefunction with angular momentum J, rotational symmetry species C_r and multiplicity index n; $\Psi^{(C_v)}_v$ is a coupled vibrational basis set; C is the overall symmetry species ($C = C_v \otimes C_r$). In the present case, $\Psi^{(C_v)}_v$ contains the relevant functions for the ν_3 or ν_4 normal modes of vibration,

$$\left| \Psi^{(C_v)}_v \right\rangle = \left| \Psi^{(v_i,l_i,n_iC_v)}_{\sigma_v} \right\rangle \tag{12}$$

with $i = 3$ or 4, v_i and l_i being the usual vibrational angular momentum quantum number for triply degenerate vibrations. In the case of the bending overtone band $2\nu_4$, we have $v_4 = 2$ and $(l_4 = 0, C_v = A_1)$, $(l_4 = 2, C_v = E)$ or $(l_4 = 2, C_v = F_2)$, corresponding to the three sublevels described above.

The effective Hamiltonian matrix is diagonalized numerically, and this leads to eigenfunctions obtained from

$$\widetilde{H}\left|\Psi_{\sigma}^{(J,C,\alpha)}\right\rangle = E\left|\Psi_{\sigma}^{(J,C,\alpha)}\right\rangle, \tag{13}$$

where $\alpha = 1, 2, \ldots$ numbers functions with the same symmetry C in a given J block. This eigenbasis set can be expanded in terms of the initial rovibrational basis set (11) and is used to calculate the matrix elements of the effective dipole moment operator $\widetilde{\mu}$. The line intensity at temperature T for a transition at wavenumber $\widetilde{\nu}_{if}$ between an initial state i (with energy E_i) and a final state f is then obtained through:

$$\begin{aligned} &S_{if}(\mathrm{cm}^{-1}/(\mathrm{molecule.cm}^{-2})) = \\ &\quad \frac{8\pi^3}{hcQ}\widetilde{\nu}_{if}e^{-\frac{E_i}{k_BT}}\left(1-e^{-\frac{hc\widetilde{\nu}_{if}}{k_BT}}\right)\sum_{\alpha_i,\alpha_f}\left|\left\langle\Psi_{\sigma_f}^{(J_i,C_i,\alpha_i)}\right|\widetilde{\mu}_Z\left|\Psi_{\sigma_f}^{(J_f,C_f,\alpha_f)}\right\rangle\right|^2, \end{aligned} \tag{14}$$

where Q is the total partition function at temperature T (calculated thanks to a simple harmonic approximation for vibration [33] and the rotational approximation for spherical-top molecules given by McDowell in Ref. [34]), c the speed of light in vacuum, h Planck's constant and k_B Boltzmann's constant. It is only needed to consider the $\widetilde{\mu}_Z$ component of the effective dipole moment in the laboratory-fixed frame [29, 31]. The line strength S_{if} is expressed here in the so-called "HITRAN unit" [28] (that is $\mathrm{cm}^{-1}/(\mathrm{molecule.cm}^{-2})$).

4. Analysis and discussion

4.1. Line positions for the ground state and ν_3 band

We started the analysis for $^{28}SiF_4$ using initial parameters for the ground and $v_3 = 1$ states taken from the paper of Jörissen *et al.* [15] and included in the STDS (*Spherical-Top Data System*) package [35], part of the XTDS (*eXtended spherical-Top Data System*) software [36]. This led to a good initial spectrum simulation that allowed to assign many ν_3 lines from our new spectrum, thanks to the SPVIEW (*Spectrum-View*) software [36]. After several fits, simulations and new assignment sets, we finally reached a total of 3728 assigned lines for ν_3 itself, up to $J = 80$ (Ref. [15] used 165 lines up to $J = 45$). For this, we used both the cold and room temperature spectra #1 to #4 described in Section 2.

We then performed a global fit of both the ground ($v = 0$) and $v_3 = 1$ state effective Hamiltonian parameters by including GS−GS, $\nu_3 - \nu_3$ and ν_3−GS data altogether.

Concerning the ground state ($v = 0$), we used 19 double resonance rotational lines with high accuracy from Jörissen *et al.* (see Table 2 of Ref. [15]). It should be noticed that this reference listed 20 such lines, since one $J = 38$ line was observed twice, without any further comment. We kept only the one with the lowest observed−calculated difference in our fit.

We also used double resonance rotational lines in the $v_3 = 1$ state from Jörissen *et al.* [15]. The list in this reference included in fact 165 lines form a previous study by Takami and Kuze [14] and 21 additional lines. However, their resulting list of 186 lines included 4 lines that were measured twice (two for $J = 21$, one for $J = 22$ and one for $J = 39$).

Again, we eliminated the ones leading to the highest observed−calculated difference in our fit, giving finally 182 highly accurate purely rotational lines for ν_3.

We obtained a very satisfying fit whose root mean square deviation is 5.7×10^{-7}, 1.3×10^{-6} and 0.219×10^{-3} cm^{-1} for GS−GS, $\nu_3-\nu_3$ and ν_3−GS transitions, respectively. Ten ground state parameters and twenty ν_3 parameters, up to order 6, could be fitted. The results are given in Table 2.

[Table 2 here.]

It was then possible to assign and fit, for the very first time, the two minor isotopologues, namely $^{29}SiF_4$ and $^{30}SiF_4$. For this, we first perform simulations using $^{28}SiF_4$ parameters that were simply shifted to place the Q branch at the correct isotopologue position, which is clearly visible in the 160 K spectrum (see Figure 1). Although the abundance of these two isotopologues is quite low, it was nevertheless relatively straightforward to assign their lines. For both of them, the GS parameters where fixed to the values of $^{28}SiF_4$, since the rotational lines, within a very good approximation, do not depend on the mass of the central isotope. Resulting $v_3 = 1$ effective Hamiltonian parameters and fit statistics for $^{29}SiF_4$ and $^{30}SiF_4$ are also given in Table 2. Parameters that could not be correctly fitted were kept fixed to $^{28}SiF_4$ values.

Figures 2 and 3 display the fit residuals for line positions for rotational ($^{28}SiF_4$) and rovibrational (all isotopologues) lines, respectively.

[Figure 2 here.]

[Figure 3 here.]

Figures 4 and 5 show simulation examples, compared to the experimental spectrum at 160 K.

[Figure 4 here.]

[Figure 5 here.]

Figure 6 shows the reduced energy levels in the case of $^{28}SiF_4$, defined by

$$\begin{aligned}\widetilde{\nu}_{\rm red} &= \widetilde{\nu} - \sum_{\Omega} t^{\Omega(0,0A_1)A_1A_1}_{\{\rm GS\}\{\rm GS\}}(J(J+1))^{\Omega/2} \\ &= \widetilde{\nu} - B_0J(J+1) + D_0J^2(J+1)^2 - \ldots, \end{aligned} \quad (15)$$

i.e. we subtract the dominant scalar polynomial terms in order to enhance levels splittings due to molecular symmetry. We give both the calculated and observed reduced energy levels. Observed levels are simply levels reached by assigned transitions which are included in the fit. This gives a good idea of the sampling of the energy spectrum. The two other isotopologues lead to a very similar picture.

4.2. Line intensities for the ν_3 band

The intensities for the ν_3 band have been determined in two ways : total integrated band intensities were measured in HR spectra corresponding to four different pressures of SiF_4 in mixtures with a small added nitrogen amount (here about 3.5 mbar) to increase the total linewidth well above the width of the apparatus function (the OPD is here 882 cm, thus the width of the sinc function is here about 0.0007 cm^{-1}). In this case, the temperature

was estimated to be 155 K. The average value is 691 ± 27 km.mol^{-1} with a 95 % confidence interval, when taking into account Student's law correction.

The second method involves fitting some relatively isolated lines using the model presented earlier with a single, first order parameter and a Herman-Wallis correction for the dipole moment, as described in Section 3.2. The pure SiF_4 sample was used to determine the line positions, and the slightly nitrogen-broadened sample was used to retrieve the line intensities for a number of isolated transitions of $^{28}SiF_4$. In the fitting procedure, a Voigt profile was used, fixing the Gaussian contribution to the expected Doppler width value at the gas temperature (155 K, spectrum #8 from Table 1). At the measurement temperature, the effective N_2 broadening parameter was on the order of 0.14 cm^{-1}.atm^{-1} at 155 K. This was estimated from the evolution of the Lorentzian component of the Voigt profiles in spectra taken at about the same SiF_4 partial pressure and varied nitrogen broadening pressures (spectra #8 and 9 in Table 1).

The line intensity retrieval involved mono-spectrum softwares: the WS software [37] was tested as well as the Bruker one, as the influence of the appartus function was found negligeable when using slight nitrogen pressure broadening. An example of the fit is given on Figure 7 for two lines of the $P(21)$ cluster in the P branch. Note that weak lines from the hot bands still remain visible, even at 155K, and reduce the precision of the measurements. For the fit, the line intensities were weighted using experimental uncertainties. These ones involve several different factors: first, those on measurement parameters such as sample purity (< 1 %), path length (< 1 %), temperature ($5/155 = 3$ %) and pressure (1.2 %), were conservatively estimated. Secondly, the uncertainty on the fitting procedure is more difficult to quantify. By varying slightly the starting guesses and shapes of the neighboring lines, we can estimate and retain an uncertainty of about 10 %. Overall, this amounts to about 10 to 20 % and is implemented in our linelist for the fit, for each line. The complete line list, including uncertainties, is provided in the Appendix.

[Table 7 here.]

We could use 83 lines to get a reasonable fit of the $\mu^0_{\nu_3}$ (dipole moment derivative) and $\mu^1_{\nu_3}$ (Herman-Wallis parameter), with a root-mean-square deviation of 5.1 %. We thus performed a simulation using a Voigt profile for all lines, at 155 K, a SiF_4 pressure of 0.226 mb and 3.606 mb of N_2. Figure 8 displays the fit residuals.

[Figure 8 here.]

Figure 9 displays the result of the comparison. For $^{29}SiF_4$ and $^{3}SiF_4$, we use the same dipole moment parameters, assuming a negligible isotopic dependence at this level of approximation. The total partition function value is $Q = 67353$ and isotopic abundance values were taken as given in the Introduction.

[Figure 9 here.]

It is possible to evaluate this result, by comparing with literature data. For the simulation of Figure 9, we thus used our effective dipole moment parameter with value:

$$\widetilde{\mu}^{0(0,A_1)A_1F_2(F_2)}_{\{GS\}\{\nu_3\}} = \mu^0_{\nu_3} = \left(\frac{\partial \mu_3}{\partial q_3}\right)_0 = 0.5444 \text{ Debye.} \quad (16)$$

Dipole moment parameter notations are not unified. In Refs. [13] and [38], respectively, the

authors use the parameter

$$|\mu_3| = \mu_{01} = \frac{\mu^0_{\nu_3}}{\sqrt{3}}., \tag{17}$$

while authors in Ref. [17] use

$$P'_3 = \mu^0_{\nu_3}. \tag{18}$$

Int Table 3, we compare our value to those of the three above-cited references. Our value agrees well with the experimental one of Patterson *et al.* [13], which we took as the mean value of their four experimental measurements obtained using four isolated lines. This is significantly higher than the calculated values given in the two other references. In the same Table, we also compare our ν_3 band integrated intensity with the values given by Burtsev *et al.* [17]. The agreement is reasonable.

[Table 3 here.]

In addition, band integrated intensities for some weak combination or overtone transitions could be measured and are compared in Table 4 to theoretical predictions made in Ref. [39] using a parametric model and the more recent measurements of Ref. [17] made at lower resolution with SiF_4 at elevated pressure. If this latter study gives reference measurements for clearly isolated transitions, the smearing of the absorptions can make intensity measurements of weaker transitions neighboring strong ones difficult.

This comparison calls for a few comments: for strong or clearly isolated bands our results are completely consistent with those of Ref. [17], but for some weak, neighboring lines ($2\nu_4$, $\nu_1 + 2\nu_2$, $\nu_3 + 2\nu_4$ for instance) our results differ by more than the error bars. The weak activity of the $\nu_1 + 2\nu_2$ transition is likely due to a rotational resonance and could not be predicted by the model of ref [39].

4.3. Line positions for the ν_4 band

In the same manner, we could analyze the ν_4 bending fundamental band. This is the first-ever detailed analysis of this band, never reported at high resolution before. Thus, there existed no previous values for the the effective Hamiltonian parameters. In this case, we fixed the ground state parameters to those obtained previously (see previous Section) for $^{28}SiF_4$ thanks to the GS/ν_3 global fit. By tuning by hand the band center, Coriolis parameter and $\Delta B_4 = B_4 - B_0$ values, it was possible to obtain an initial simulation allowing to assign the spectrum using SPVIEW [36].

As a second step, the ν_4 assignments we included in a global fit with the $2\nu_4$ lines described in the next Section. We got an excellent fit of 22 effective Hamiltonian parameters for $^{28}SiF_4$, with a root mean square deviation of 0.261×10^{-3} cm^{-1} for 4166 assignments up to $J = 72$. It was then possible to assign and fit the ν_4 band of $^{29}SiF_4$ and $^{30}SiF_4$ isotopologues (without $2\nu_4$ in this case). Table 2 summarizes the results. As in the case of ν_3, parameters that could not be correctly fitted were kept fixed to $^{28}SiF_4$ values. For this band, no attempt to study absolute line intensities was performed.

Fit residuals for line positions are shown in Figure 10. We can observe some small systematic polynomial deviation at high J values (lower end of the P branch and upper end of the R branch). However, no higher order parameter could be properly fitted. This may

indicate some perturbation, maybe through an interaction with the ν_2 bending fundamental band. This cannot be confirmed at this stage, since this band has not yet been observed at high resolution (see Conclusion of this paper below).

[Figure 10 here.]

Figure 11 compares the simulation to the experiment and Figure 12 shows the observed and calculated reduced energy levels, as for ν_3 (see explanation in the previous Section).

[Figure 11 here.]

[Figure 12 here.]

4.4. Line positions for the $2\nu_4$ band

Finally, we could also assign and fit the $2\nu_4$ overtone band of $^{28}SiF_4$ for the first time. For this we used the effective Hamiltonian given by Eq. (7). $H_{\{GS\}}^{<2\nu_4>}$ and $H_{\{\nu_4\}}^{<2\nu_4>}$ parameters have been at first fixed to the values of the previous Sections (GS values from the GS/ν_3 global fit and ν_4 values from the ν_4-only fit). By tuning by hand the anharmonicity values for the three vibrational sublevels (*i.e* the purely vibrational parameters of $H_{\{2\nu_4\}}^{<2\nu_4>}$), it was possible to start line assignments. Then we performed a global fit of $v_4 = 1$ and $v_4 = 2$ parameters together. The resulting ν_4 parameters for $^{28}SiF_4$ are reported in Table 2, as explained before. Concerning $2\nu_4$, we could fit 15 additional parameters, for 505 assignments up to $J = 59$ with a root mean square deviation of 0.967×10^{-3} cm^{-1}. The results are given in Table 5. The A_1, E and F_2 sublevels are lying at 776.895, 777.433 and 777.063 cm^{-1}, respectively. We can notice that Heenan [40] calculated the position of the A_1 sublevel at 776.57 cm^{-1} (ν^* value in Table 9c of this reference) from force-field calculations and fitted it to 776.86 cm^{-1} (Table 9b of this reference).

[Table 5 here.]

Fit residuals for line positions are shown in Figure 13. Figure 14 compares the simulation to the experiment and Figure 15 shows the observed and calculated reduced energy levels.

[Figure 13 here.]

[Figure 14 here.]

[Figure 15 here.]

Due to the weakness of the spectrum, it was not possible to analyze the $2\nu_4$ spectrum of $^{29}SiF_4$ and $^{30}SiF_4$.

4.5. Isotopic dependence for the band centers and Coriolis coupling parameters

Recently, we published a study of approximate isotopic relations for band centers and Coriolis parameters for tetrahedral and octahedral spherical-top molecules [25]. Here, we apply exactly the same theory to SiF_4. The results are shown in Figure 16, which is similar to Figure 2 of Ref. [25] concerning germane, GeH_4. The reader can refer to this paper for detailed explanations. We can see that this simple extrapolation works well, giving reasonably small errors. As for the examples given in Ref. [25], the best results are obtained by taking for the ζ_4 Coriolis parameter the value $1 - \zeta_3^{exp}$, since the $\zeta_3 + \zeta_4 = 1/2$ sum rule [41] is not accurately respected for the effective Hamiltonian parameters (around 0.49 for all isotopologues, instead of 0.5). We also recall that, following Refs. [42, 29], our tensorial

formalism Coriolis parameter is related to the "usual" ζ_i ($i = 3$ or 4) constant through:

$$t^{1(1,0F_1)}_{\{i\}\{i\}} = 3\sqrt{2}(B\zeta)_i. \tag{19}$$

We use this relation to estimate the ζ_i value, with the approximation

$$(B\zeta)_i \simeq B_0\zeta_i, \tag{20}$$

B_0 being the ground state rotational constant. Using the values from Table 2, we find $\zeta_3 \simeq 0.5357$ and $\zeta_4 \simeq -0.047$ for $^{28}SiF_4$. This is to be compared to the old values of Clark and Rippon [11], that are $0.53 \leq \zeta_3 \leq 0.63$ and $-0.08 \leq \zeta_4 \leq -0.06$. We can notice that Heenan had inverted these values [40].

Another approximation for this little study is that, since we do not know at this stage the anharmonicity constants for the ν_3 and ν_4 mode, then the harmonic wavenumber ω_i ($i = 3$ or 4) is approximated by the fitted band center ν_i from Table 2. For the other examples given in Ref. [25], this has proved to be a reasonable approximation, leading to correct relative isotopic shifts.

[Figure 16 here.]

We find respective isotopic shifts for the ν_3 and ν_4 band centers of $\Delta\nu_3 \simeq -8.70$ cm^{-1}/amu and $\Delta\nu_4 \simeq -1.48$ cm^{-1}/amu (where amu stands for "atomic mass unit"). A long time ago, in his thesis, Heenan (Table 9b of Ref. [40]) reported mean calculated values of $\Delta\nu_3 \simeq -8.85$ cm^{-1}/amu and $\Delta\nu_4 \simeq -1.32$ cm^{-1}/amu, which is very comparable.

5. The TFSiCaSDa database

We have set up a new database of calculated lines for the ν_3 stretching fundamental (the only one for which we can estimate absolute line intensities at present, thanks to the results presented in Section 4.2). It is named TFSiCaSDa (Tetra-Fluoro Silicon Calculated Spectroscopic Database), and contains data for the three isotopologues of SiF_4. So far, data are accessible through the following url: `https://vamdc.icb.cnrs.fr/PHP/SiF4.php`, in the HITRAN2004 output format [43]. A total of 63 068 synthetic lines, in the range [993.9 cm^{-1}, 1049.3 cm^{-1}] and for line intensities higher than 10^{-23}cm^{-1}/molecule.cm^{-2}, have been collected in the database. They are represented in Figure 17.

[Figure 17 here.]

Concerning line widths, we suggest to use an approximate air broadening coefficient $\gamma_{\rm air} = 0.073$ cm^{-1}/atm (based on a value of 1 for the temperature exponent).

Finally, TFSiCaSDa should be accessible through the VAMDC (*Virtual Atomic and Molecular Data Centre*) portal [44, 45, 46] in the near future.

6. Conclusion

We have presented here the first detailed analysis of high-resolution spectra for the three isotopologues of SiF_4, including the ground state, $v_3 = 1$, $v_4 = 1$ and $v_4 = 2$ states. For $^{28}SiF_4$ itself, a global fit of the ground state, $\nu_3 - \nu_3$ and ν_3 bands on the one hand and of

the ν_4 and $2\nu_4$ bands on the other hand have been performed. A fit of the ν_3 dipole moment derivative and an estimate of the integrated band intensity is provided for $^{28}SiF_4$. We could also study the band center and Coriolis coupling parameter isotopic dependence for the ν_3 and ν_4 normal modes. A database of calculated lines in the ν_3 region for both isotopologues has been set up.

However, some more work is still necessary to fully and quantitatively model the absorption in the ν_3 stretching region, which is the strongly absorbing atmospheric region used to monitor SiF_4's abundance. As a matter of fact, this quite heavy molecule has many low-lying vibrational states, which are populated at room temperature (the ground state population at 296 K being only 30.7 %, while it is 74.9 % at 160 K, explaining why we barely see any hot band in our cold spectra), as illustrated by Figure 18.

[Figure 18 here.]

In order to model the resulting hot bands in the ν_3 region, it is now necessary to study other vibrational states. Contrary to other tetrahedral molecules, the four fundamental bands are relatively isolated (we did not observe strong perturbations in the ν_3 spectrum, but likely a small one in the case of the ν_4 band at high J values, see Section 4.3). Thus, the ν_1 and ν_2 modes are not accessible through couplings with ν_3 and ν_4, as in methane [47] or germane [48]. We thus intend to reach these states through difference bands in the far-infrared regions, as for SF_6 [49]. This will give the main lower states of hot bands. Upper states of hot bands can be analyzed through combination bands. We already have high-resolution spectra for some of them, as illustrated in Figure 19. Their detailed analysis also requires the prior study of ν_1 and ν_2.

[Figure 19 here.]

7. Acknowledgments

The authors thank the CNRS and SOLEIL for support (project 99160223).

Appendix: Line list for the intensity fit of $^{28}SiF_4$

Table 6 gives the observed and calculated line positions and line intensities for the 83 transitions used in the intensity fit described in Section 4.2. Line intensities are given in $cm^{-2}.atm^{-1}$ at 155 K, as used by the XTDS software [36]. In this table, ΔI_{exp} is the relative error for experimental measurements (see Section 4.2), while ΔI_{fit} is the relative fit residual:

$$\Delta I_{fit} = 100 \frac{I_{exp} - I_{calc}}{I_{exp}}. \quad (21)$$

References

[1] P. Francis, C. Chaffin, A. Maciejewski, C. Oppenheimer, Remote determination of SiF_4 in volcanic plumes: A new tool for volcano monitoring, Geophys. Res. Lett. 23 (1996) 249–242.

[2] E. Nicotra, M. Viccaro, C. Ferlito, R. Cristofolini, Influx of volatiles into shallow reservoirs at Mt. Etna volcano (Italy) responsible for halogen-rich magmas, Eur. J. Mineral. 22 (2010) 121–138.

[3] W. Stremme, I. Ortega, C. Siebe, M. Grutter, Gas composition of Popocatépelt volcano between 2007 and 2008: FTIR spectroscopic measurements of an explosive event during quiescent degassing, Earth Plan. Sc. Lett. 301 (2011) 502–510.
[4] W. Stremme, A. Krueger, R. Harig, M. Grutter, Volcanic SO_2 and SiF_4 visualization using 2-D thermal emission spectroscopy – Part 1: Slant-columns and their ratios, Atmos. Meas. Tech. 5 (2012) 275–288.
[5] A. Krueger, W. Stremme, R. Harig, M. Grutter, Volcanic SO_2 and SiF_4 visualization using 2-D thermal emission spectroscopy – Part 2: Wind propagation and emission rates, Atmos. Meas. Tech. 6 (2013) 47–61.
[6] N. Taquet, W. Stremme, M. Grutter, J. Baylón, A. Bezanilla, B. Schiavo, C. Rivera, R. Campion, T. Boulesteix, A. Nieto-Torres, R. Espinasa-Pereña, T. Blumenstock, F. Hase, Variability in the gas composition of the Popocatépelt volcano plume, Front. Earth Sci. 7 (2019) 114–1–114–14.
[7] T. Mori, M. Sato, Y. Shimoike, K. Notsu, High SiF_4/HF ratio detected in Satsuma-Iwojima volcano's plume by remote FT-IR observation, Earth Plan. Sp. 54 (2002) 249–256.
[8] N. Taquet, I. Meza Hernández, W. Stremme, A. Bezanilla, M. Grutter, R. Campion, M. Palm, T. Boulesteix, Continous measurements of SiF_4 and SO_2 by thermal emission spectroscopy: Insight from a 6-month survey at the Popocatépelt volcano, J. Volcanol. Geotherm. Res. 341 (2017) 255–268.
[9] L. Schaefer, B. Fegley Jr., Silicon tetrafluoride on Io, Icarus 179 (2005) 252–258.
[10] T. Shimanouchi, I. Nakagawa, J. Hiraishi, M. Ishii, Force constants of CF_4, SiF_4, BF_3, CH_4, SiH_4, NH_3 and PH_3, J. Mol. Spectrosc. 19 (1966) 78–107.
[11] R. Clark, D. Rippon, The vapor-phase Raman spectra, Raman band contour analyses, Coriolis constants, and force constants of spherical-top molecules MX_4 (M = Group IV element, X = F, Cl, Br or I), J. Mol. Spectrosc. 44 (1972) 479–503.
[12] F. Königer, A. Müller, Molecular constants of SiF_4, GeF_4 and RuO_4. An improvement and the analysis of the IR-band contours of $\nu_3(F_2)$ low temperature measurements and by using isotopically pure compounds, J. Mol. Spectrosc. 65 (1977) 339–344.
[13] C. W. Patterson, R. S. McDowell, N. G. Nereson, B. J. Krohn, J. S. Wells, F. R. Petersen, Tunable laser diode study of the ν_3 band of SiF_4 near 9.7 μm, J. Mol. Spectrosc. 91 (1982) 416–423.
[14] M. Takami, H. Kuze, Infrared-microwave double resonance spectroscopy of the SiF_4 ν_3 fundamental using a tunable diode laser, J. Chem. Phys. 78 (1983) 2204–2209.
[15] L. Jörissen, H. Prinz, W. A. Kreiner, C. Wenger, G. Pierre, G. Magerl, W. Schupita, The ν_3 fundamental of silicon tetrafluoride. Spectroscopy with laser sidebands, Can. J. Phys. 67 (1989) 532–542.
[16] C. W. Patterson, A. S. Pine, Doppler-limited spectrum and analysis of the $3\nu_3$ manifold of SiF_4, J. Mol. Spectrosc. 96 (1982) 404–421.
[17] A. P. Burtsev, V. N. Bocharov, S. K. Ignatov, T. D. Kolomiĭtsova, P. G. Sennikov, K. G. Tokhadze, L. A. Chuprov, D. N. Shchepkin, O. Schrems, Integral intensities of absorption bands of silicon tetrafluoride in the gas phase and cryogenic solutions: Experiment and Calculation, Optics Spectrosc. 98 (2005) 227–234.
[18] O. Pfister, F. Guernet, G. Charton, C. Chardonnet, CO_2-laser sideband spectroscopy at ultrahigh resolution, J. Opt. Soc. Am. B 10 (1993) 1521–1525.
[19] L. Halonen, Stretching vibrational overtone and combination states in silicon tetrafluoride, J. Mol. Spectrosc. 120 (1986) 175–184.
[20] L. Jörissen, W. A. Kreiner, Y.-T. Chen, T. Oka, Observation of ground state rotational transitions in silicon tetrafluoride, J. Mol. Spectrosc. 120 (1986) 233–235.
[21] A. Behrendt, L. Jörissen, W. A. Kreiner, M. Loëte, Double-modulation sideband spectroscopy: μ_0 and μ_{33} of silicon tetrafluoride, J. Mol. Spectrosc. 155 (1992) 326–323.
[22] A. Ainetschian, W. A. Kreiner, M.-P. Coquard, M. Loëte, Sideband double modulation: The ground state dipole moment of SiF_4, J. Mol. Spectrosc. 161 (1993) 264–268.
[23] L. Jörissen, H. Prinz, W. A. Kreiner, Second-order Stark effect observation in the ground state of silicon tetrafluoride, SiF_4, J. Mol. Spectrosc. 124 (1987) 236–239.
[24] M.-P. Coquard, M. Loëte, A. Ainetschian, W. Kreiner, Prediction and observation of the nonlinear Stark effect in the ν_3 band of SiF_4, J. Mol. Spectrosc. 170 (1995) 251–265.

[25] M. Loëte, C. Richard, V. Boudon, Isotopic relations for tetrahedral molecules, J. Mol. Struct. 1206 (2020) 127729.
[26] A. Anantharajah, F. K. Tchana, L.Manceron, M. N. J.-M. Flaud, X. Landsheere, Integrated band intensities and absorption cross sections of phosgene (Cl_2CO) in the mid-infrared at 199, 250 and 300 K, J. Quant. Spectrosc. Radiat. Transfer 234 (2019) 71–77.
[27] M. Faye, M. Bordessoule, B. Kanouté, J.-B. Brubach, P. Roy, L.Manceron, Improved mid infrared detector for high spectral or spatial resolution and synchrotron radiation use, Rev. Sci. Inst. 87 (2016) 063119.
[28] I. E. Gordon, L. S. Rothman, R. V. C. Hill and, Y. Tan, P. F. Bernath, M. Birk, V. Boudon, A. Campargue, K. V. Chance, B. J. Drouin, J.-M. Flaud, R. R. Gamache, J. T. Hodges, D. Jacquemart, V. I. Perevalov, A. Perrin, K. P. Shine, M.-A. H. Smith, J. Tennyson, G. C. Toon, H. Tran, V. G. Tyuterev, A. Barbe, A. Csaszar, M. V. Devi, T. Furtenbacher, J. J. Harrison, A. Jolly, T. Johnson, T. Karman, I. Kleiner, A. A. Kyuberis, J. Loos, O. M. Lyulin, S. T. Massie, S. N. Mikhailenko, N. Moazzen-Ahmadi, H. S. P. Müller, O. V. Naumenko, A. V. Nikitin, O. L. Polyansky, M. Rey, M. Rotger, S. Sharpe, K. Sung, E. Starikova, S. A. Tashkun, J. V. Auwera, G. Wagner, J. Wilzewski, P. Wcisło, S. Yu, E. J. Zak, The HITRAN2016 Molecular Spectroscopic Database, J. Quant. Spectrosc. Radiat. Transfer 203 (2017) 3–69.
[29] J.-P. Champion, M. Loëte, G. Pierre, Spherical top spectra, in: K. N. Rao, A. Weber (Eds.), Spectroscopy of the Earth's atmosphere and interstellar medium, Academic Press, San Diego, 1992, pp. 339–422.
[30] V. Boudon, J.-P. Champion, T. Gabard, M. Loëte, F. Michelot, G. Pierre, M. Rotger, C. Wenger, M. Rey, Symmetry-adapted tensorial formalism to model rovibrational and rovibronic spectra of molecules pertaining to various point groups, J. Mol. Spectrosc. 228 (2004) 620–634.
[31] V. Boudon, J.-P. Champion, T. Gabard, M. Loëte, M. Rotger, C. Wenger, Spherical top theory and molecular spectra, in: M. Quack, F. Merkt (Eds.), Handbook of High-Resolution Spectroscopy, Vol. 3, Wiley, Chichester, West Sussex, United Kingdom, 2011, pp. 1437–1460.
[32] J. Vander Auwera, S. Reymond-Laruinaz, V. Boudon, D. Doizi, L. Manceron, Line intensity measurements and analysis in the ν_3 band of ruthenium tetroxide, J. Quant. Spectrosc. Radiat. Transfer 204 (2018) 103–111.
[33] D. Jackson, Statistical thermodynamic properties of hexafluoride molecules, Informal report LA-6025-MS, Los Alamos National Laboratory (1975).
[34] R. McDowell, Rotational partition function for spherical-top molecules, J. Quant. Spectrosc. Radiat. Transfer 38 (1987) 337–346.
[35] C. Wenger, J.-P. Champion, Spherical top data system (STDS) software for the simulation of spherical top spectra, J. Quant. Spectrosc. Radiat. Transfer 59 (1998) 471–480.
[36] C. Wenger, V. Boudon, M. Rotger, J. P. Sanzharov, J. P. Champion, XTDS and SPVIEW: Graphical tools for the analysis and simulation of high-resolution molecular spectra, Journal of Molecular Spectroscopy 251 (2008) 102–113.
[37] M. R. Carleer, A Windows program to accurately measure the line intensities of high-resolution Fourier transform spectra. Remote sensing of clouds and the atmosphere, Proc. SPIE, V 4168 (2001) 337–343.
[38] K. Fox, W. B. Person, Transition moments in infrared-active fundamentals of spherical-top molecules, J. Chem. Phys. 64 (1976) 5218–5221.
[39] X. W. Hou, M. Xie, S. H. Dong, Z. Q. Ma, Overtone spectra and intensities of tetrahedral molecules in Boson realization models, Ann. Phys. 263 (1998) 340–352.
[40] R. K. Heenan, The molecular structures of BrF_5 and IF_5; and vibrational potentials for some spherical top molecules, Ph.D. thesis, Department of Chemistry, University of Reading (1980).
[41] R. McDowell, Vibrational-rotational angular-momentum coupling in spherical-top molecules. II. General zeta sums., J. Chem. Phys. 43 (1965) 319–323.
[42] A. Robiette, D. Gray, F. Birss, The effective vibration-rotation Hamiltonian for triply-degenerate fundamentals of tetrahedral XY_4 molecules, Mol. Phys. 32 (1976) 1591–1607.
[43] L. S. Rothman, D. Jacquemart, A. Barbe, D. C. Benner, M. Birk, L. R. Brown, M. R. Carleer, C. C.

Jr., K. Chance, L. H. Coudert, V. Dana, V. M. Devi, J.-M. Flaud, R. R. Gamache, A. Goldman, J.-M. Hartmann, K. W. Jucks, A. G. Maki, J.-Y. Mandin, S. T. Massie, J. Orphal, A. Perrin, C. P. Rinsland, M. A. H. Smith, J. Tennyson, R. N. Tolechov, R. A. Toth, J. Vander Auwera, P. Varanasi, G. Wagner, The HITRAN 2004 molecular spectroscopic database, J. Quant. Spectrosc. Radiat. Transfer 96 (2005) 139–204.

[44] M. L. Dubernet, V. Boudon, J. L. Culhane, M. S. Dimitrijevic, A. Z. Fazliez, C. Joblin, F. Kupka, G. Leto, P. L. Sidaner, P. A. Loboda, H. E. Mason, N. J. Mason, C. Mendoza, G. Mulas, T. J. Millar, L. A. Nuñez, V. I. Perevalov, N. Piskunov, Y. Ralchenko, G. Rixon, L. S. Rothman, E. Roueff, T. A. Ryabchikova, A. Ryabtsev, S. Sahal-Bréchot, B. Schmitt, S. Schlemmer, J. Tennyson, V. G. Tyuterev, N. A. Walton, V. Wakelam, C. J. Zeippen, Virtual atomic and molecular data centre, J. Quant. Spectrosc. Radiat. Transfer 111 (2010) 2151–2159.

[45] M. L. Dubernet, B. K. Antony, Y. A. Ba, Y. L. Babikov, K. Bartschat, V. Boudon, B. J. Braams, H.-K. Chung, F. Daniel, F. Delahaye, G. D. Zanna, J. de Urquijo, A. Domaracka, M. Doronin, B. J. Drouin, M. S. Dimitrijevic, C. P. Endres, E. Quintas-Sanchez, A. Z. Fazliev, S. V. Gagarin, I. E. Gordon, U. Heiter, C. Hill, D. Jevremovic, C. Joblin, A. Kasprzak, E. Krishnakumar, G. Leto, P. A. Loboda, T. Louge, S. Maclot, B. P. Marinkovic, A. Markwick, T. Marquart, H. E. Mason, N. J. Mason, C. Mendoza, A. A. Mihajlov, T. J. Millar, N. Moreau, G. Mulas, G. Leto, Y. Pakhomov, P. Palmeri, S. Pancheshnyi, V. I. Perevalov, N. Piskunov, J. Postler, P. Gratier, P. Quinet, G. Rixon, Y. Ralchenko, Y.-J. Rhee, L. S. Rothman, E. Roueff, T. Ryabchikova, S. Sahal-Bréchot, P. Scheier, S. Schlemmer, B. Schmitt, E. Stempels, J. Tennyson, V. G. Tyuterev, V. Vujcic, V. Wakelam, N. A. Walton, O. Zatsarinny, C. J. Zeippen, C. M. Zwolf, the VAMDC Consortium, The Virtual Atomic and Molecular Data Centre (VAMDC) consortium for astrophysics, Journal of Physics B 49 (2016) 074003–1–074003–18.

[46] N. Moreau, C. M. Zwolf, Y. A. Ba, C. Richard, V. Boudon, M.-L. Dubernet, The VAMDC Portal as a major enabled of atomic ans molecular data citation, Galaxies 6 (2018) 105.

[47] A. V. Nikitin, V. Boudon, C. Wenger, S. Albert, L. R. Brown, S. Bauerecker, M. Quack, High resolution spectroscopy and the first global analysis of the Tetradecad region of methane $^{12}CH_4$, Phys. Chem. Chem. Phys. 15 (2013) 10071–10093.

[48] V. Boudon, T. Grigoryan, F. Philipot, C. Richard, F. Kwabia Tchana, L. Manceron, A. Rizopoulos, J. Vander Auwera, T. Encrenaz, Line positions and intensities for the ν_3 band of 5 isotopologues of germane for planetary applications, J. Quant. Spectrosc. Radiat. Transfer 205 (2018) 174–183.

[49] M. Faye, A. L. Ven, V. Boudon, L. Manceron, P. Asselin, P. Soulard, F. Kwabia Tchana, P. Roy, High-resolution spectroscopy of difference and combination bands of SF_6 to elucidate the $\nu_3 + \nu_1 - \nu_1$ and $\nu_3 + \nu_2 - \nu_2$ hot band structures in the ν_3 region, Mol. Phys. 112 (2014) 2504–2514.

Figures

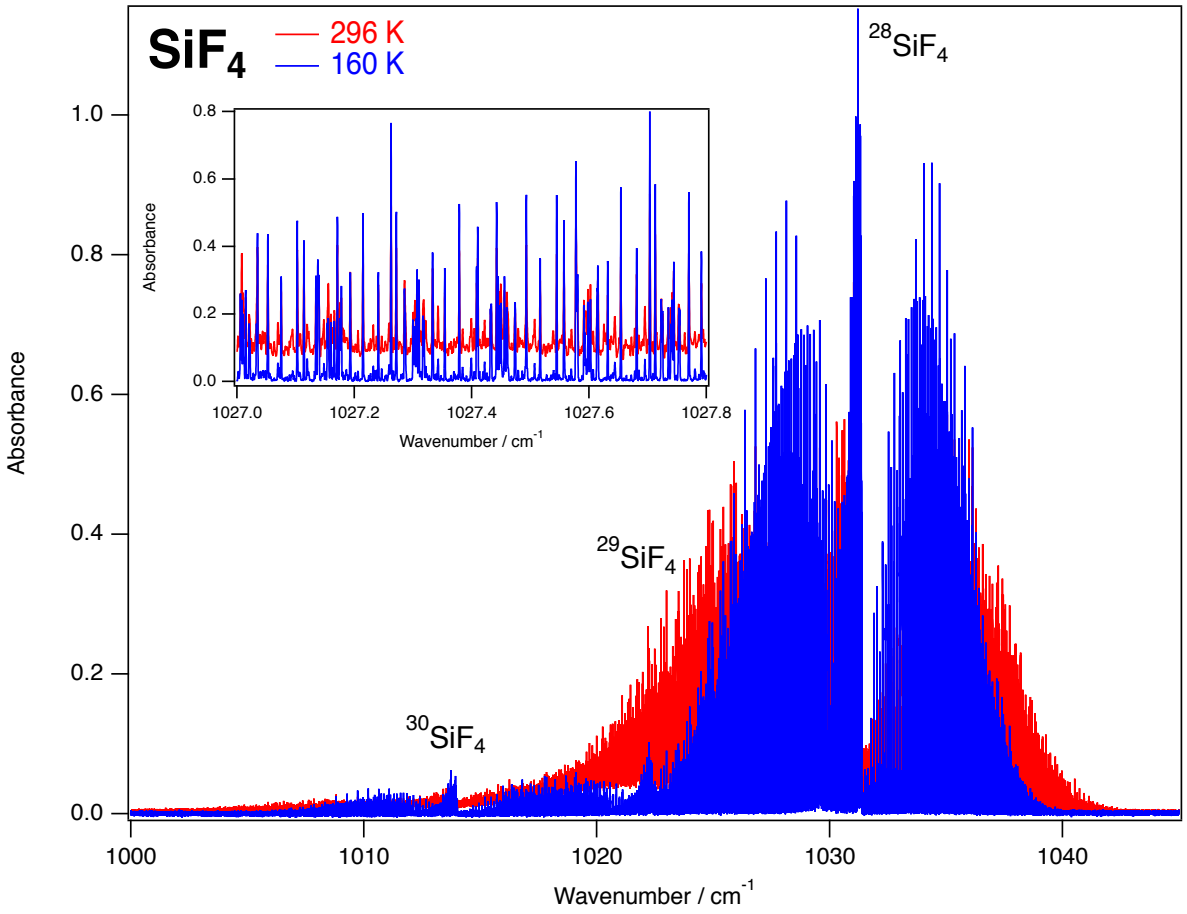

Figure 1: Examples of two experimental spectra for the ν_3 region, recorded at 160 K (spectrum #1) and 296 K (spectrum #2). The insert details a part of the P branch of $^{28}SiF_4$. The Q branch for the different isotopologues is indicated.

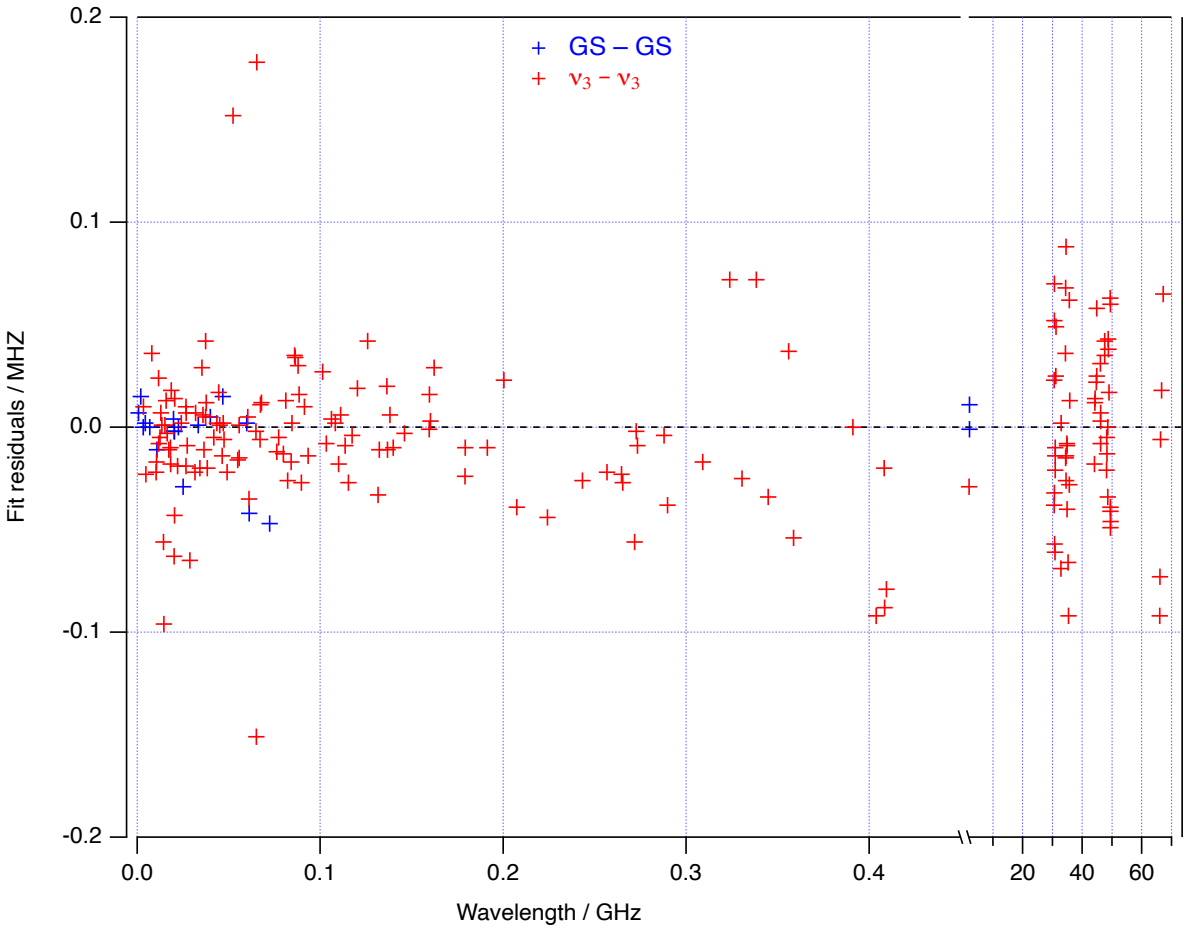

Figure 2: Observed−calculated line positions for the GS−GS and $\nu_3 - \nu_3$ rotational lines.

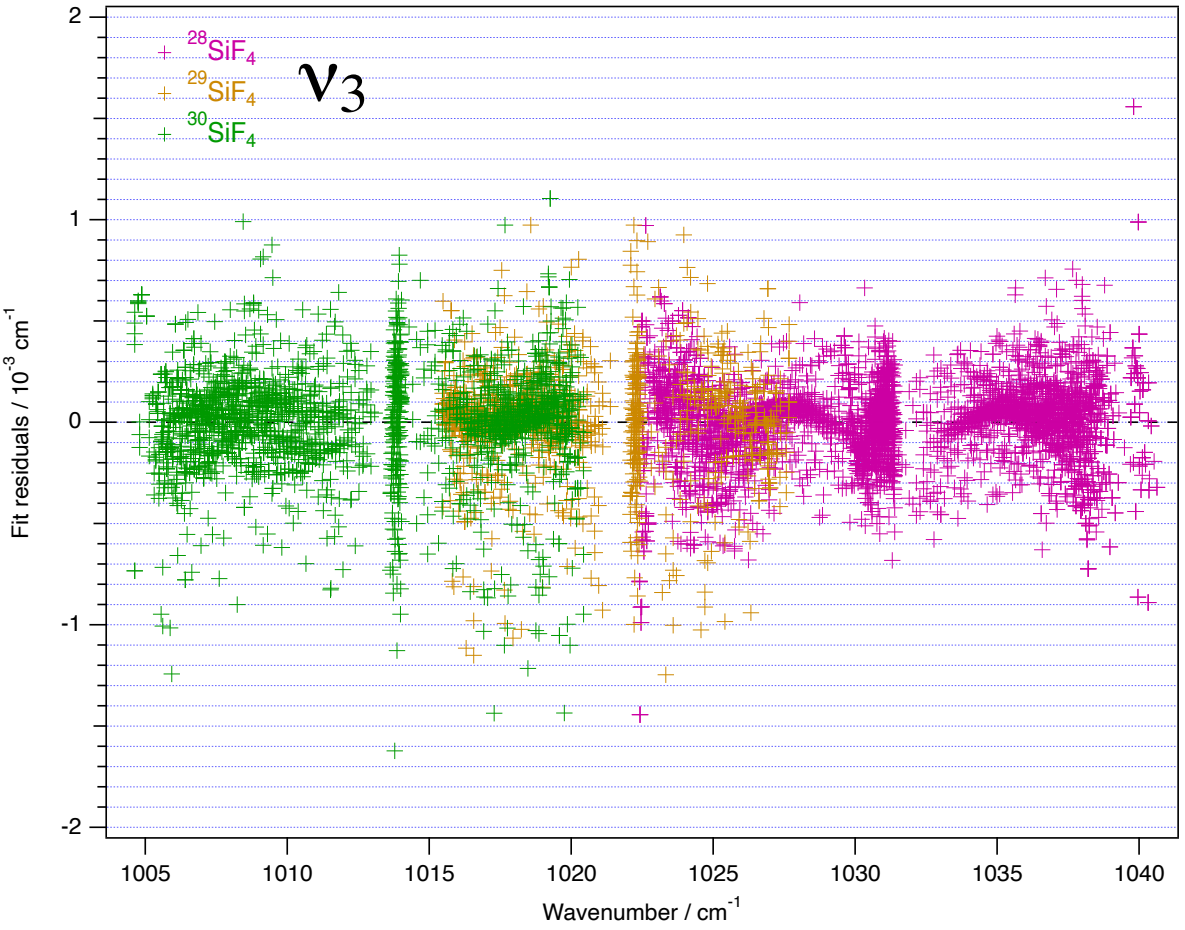

Figure 3: Observed−calculated line positions for the ν_3−GS rovibrational lines.

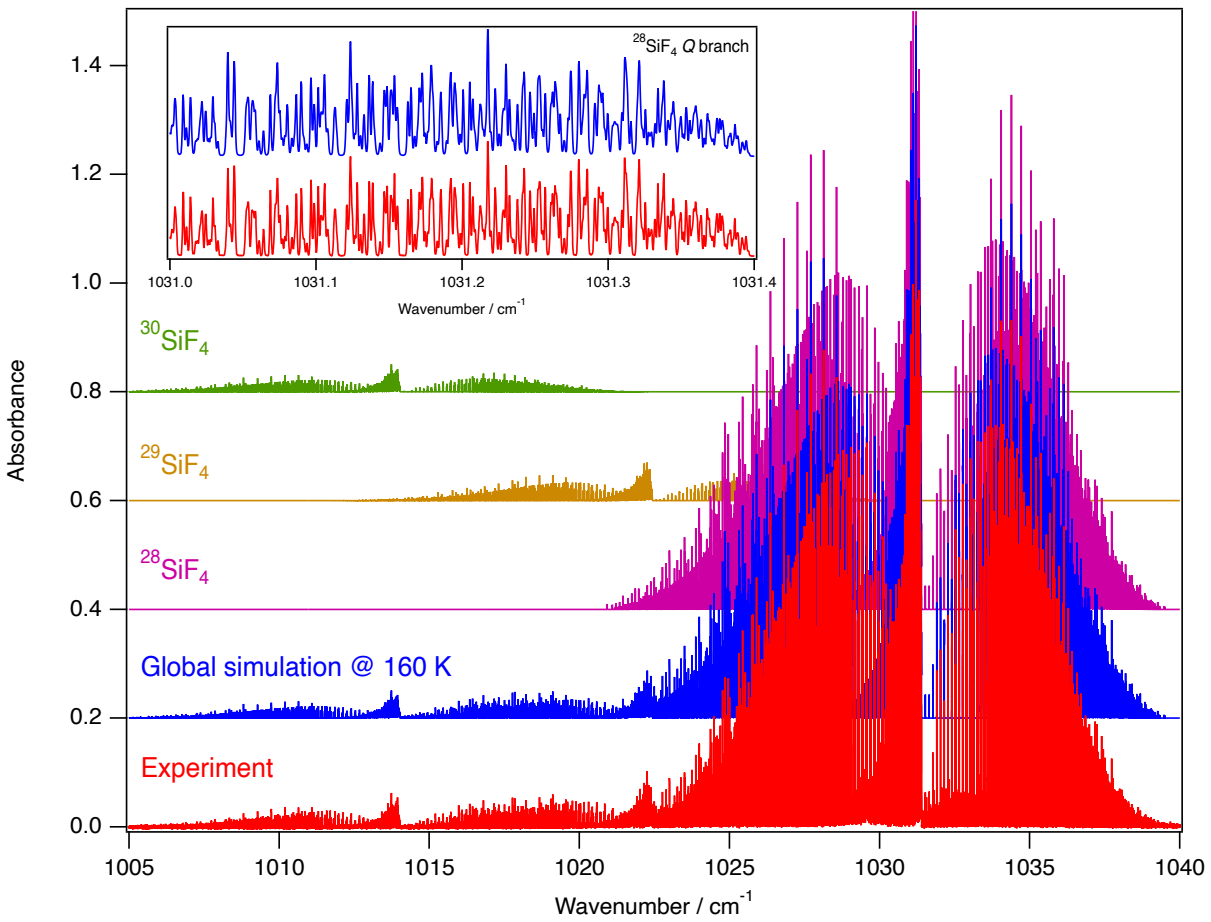

Figure 4: Overview of the ν_3 spectrum (spectrum #2), compared to the simulation for all isotopologues. The insert details a part of the Q branch region.

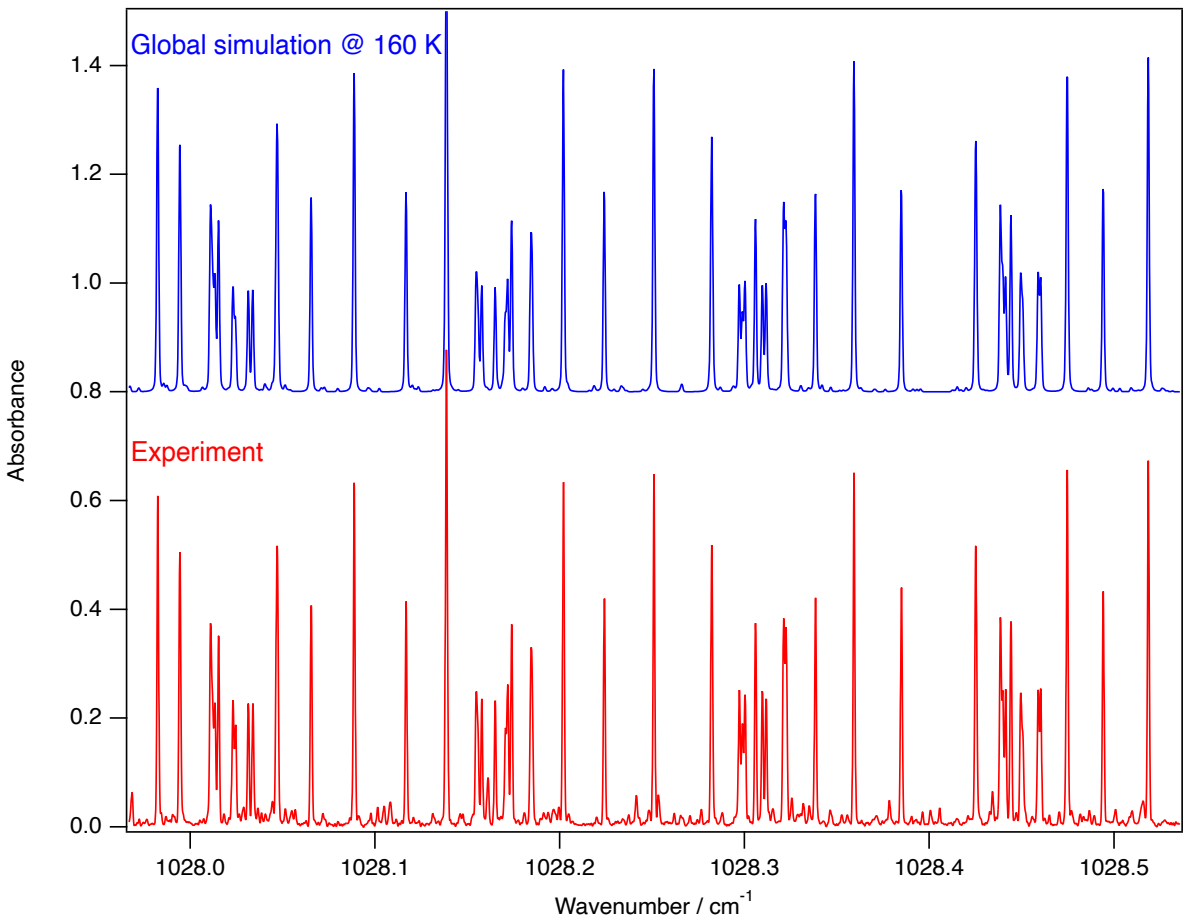

Figure 5: Detail in the P branch of the ν_3 spectrum (spectrum #2), compared to the simulation for $^{28}SiF_4$.

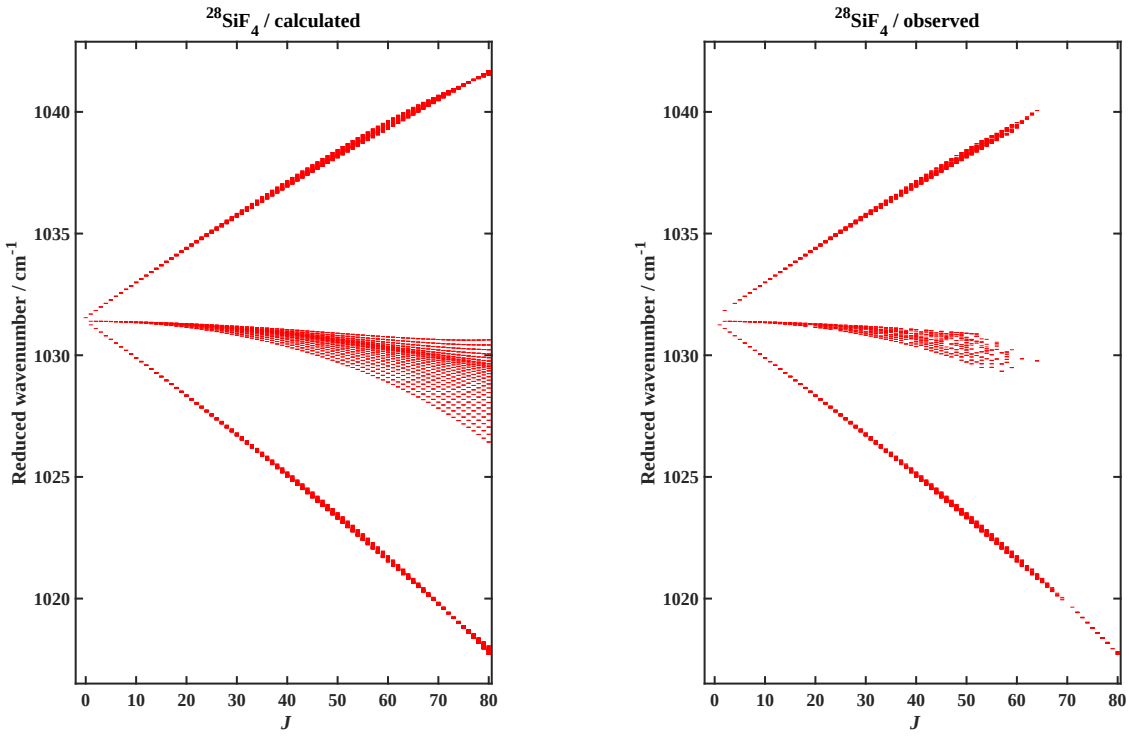

Figure 6: Observed and calculated reduced rovibrational energy levels in the $v_3 = 1$ state for $^{28}SiF_4$. Observed levels are those reached by assigned transitions.

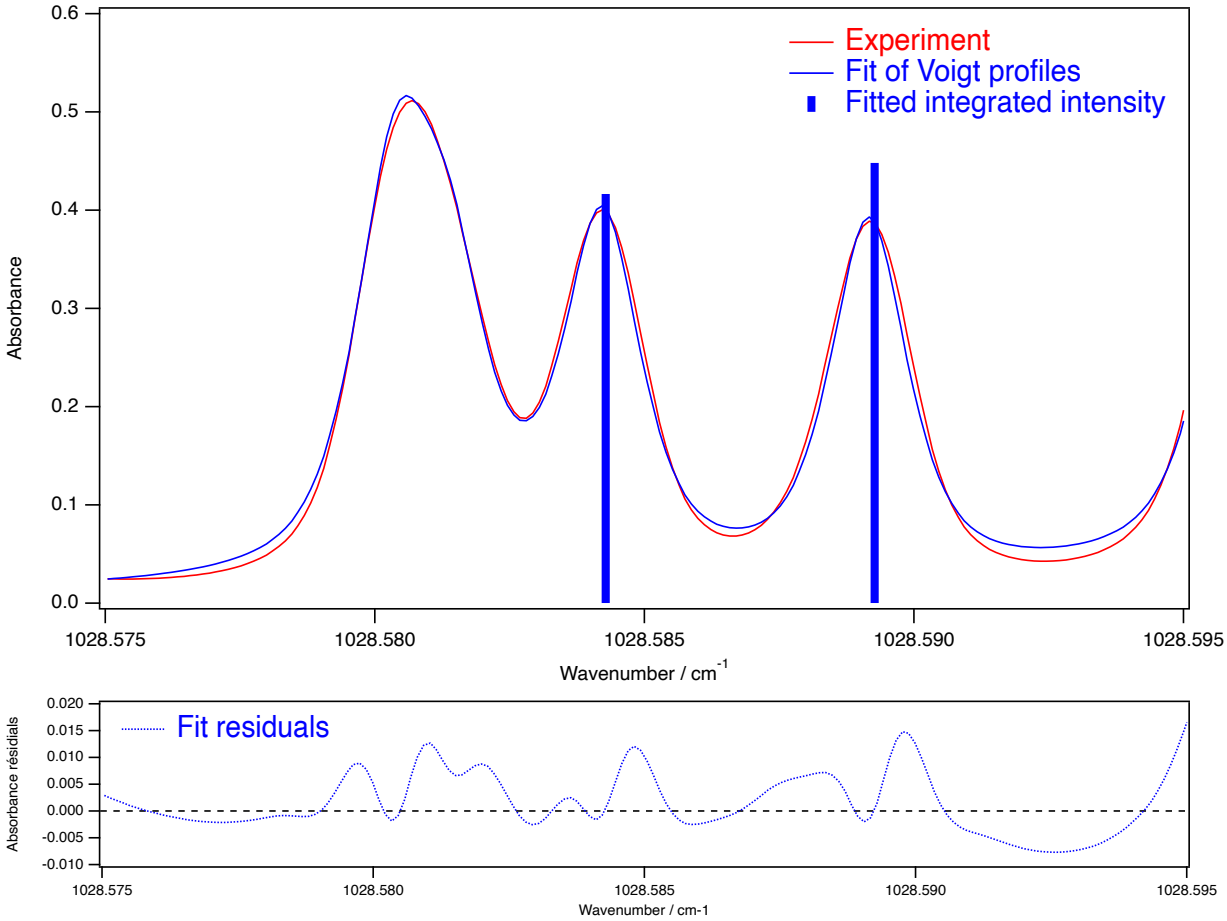

Figure 7: Comparison of experimental spectrum (#8) recorded at 155 K and fit of two observed lines of the $P(21)$ cluster. A Voigt line profile is supposed, with Gaussian contributions fixed at the Doppler broadening for all lines. The heights of the two bars represent the relative intensities of the two lines used in this region. The other lines do not correspond to isolated lines. The bottom trace presents the fit residual. Note that several weak lines from hot bands are present and not modeled here.

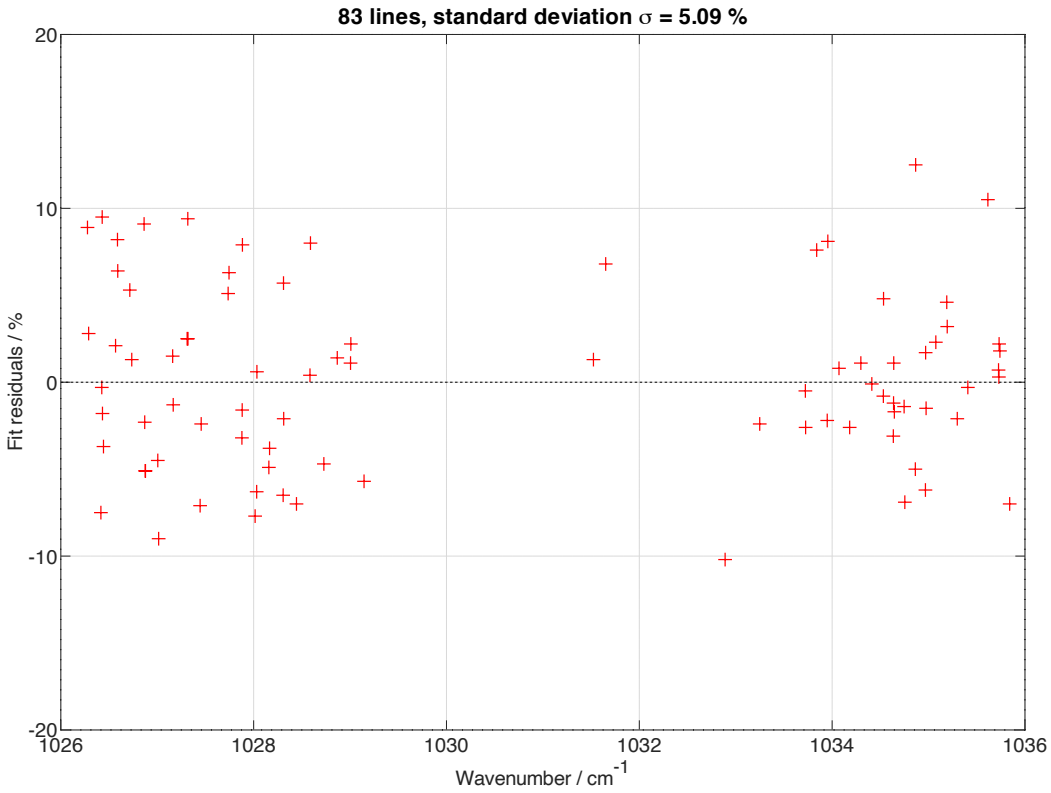

Figure 8: Observed−calculated line intensities for the ν_3 band of $^{28}SiF_4$ (relative residuals in %).

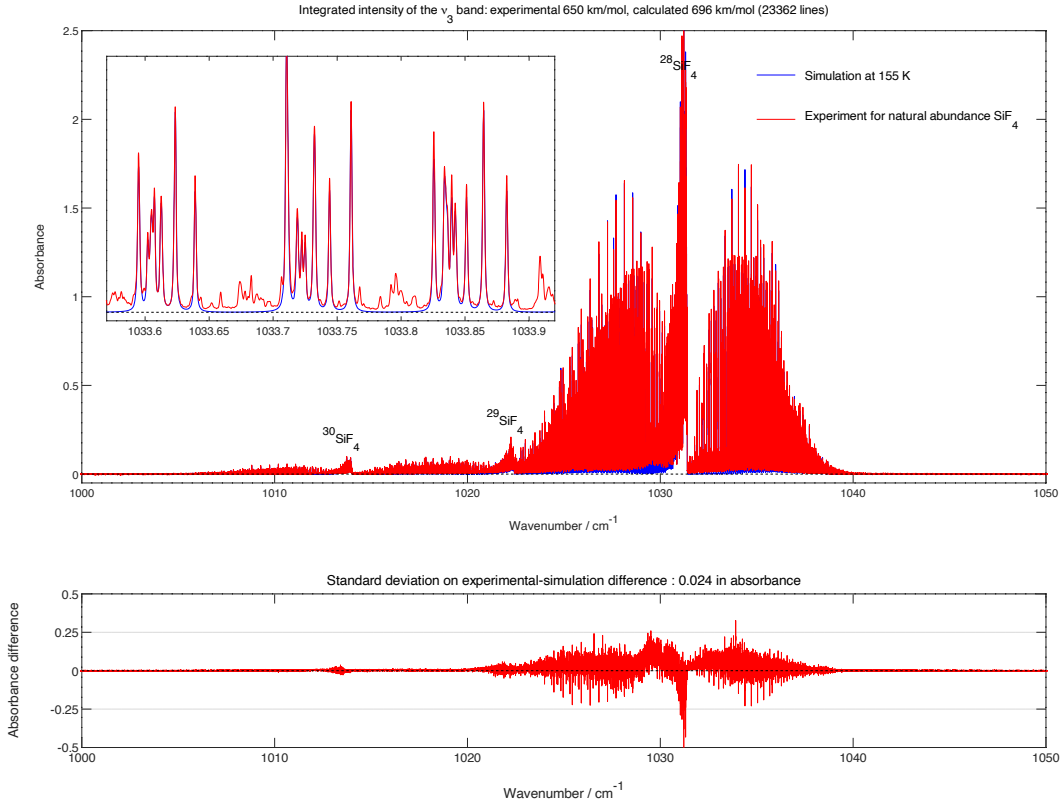

Figure 9: Simulation of the ν_3 stretching region spectrum, compared to the experiment (spectrum #5) for all isotopologues at 155 K, with determination of the integrated intensity. The insert details a part of the R branch of $^{28}SiF_4$. The lower panel displays the observed-calculated spectrum. A significant contribution to the difference comes from the hot bands which are not present in the simulation.

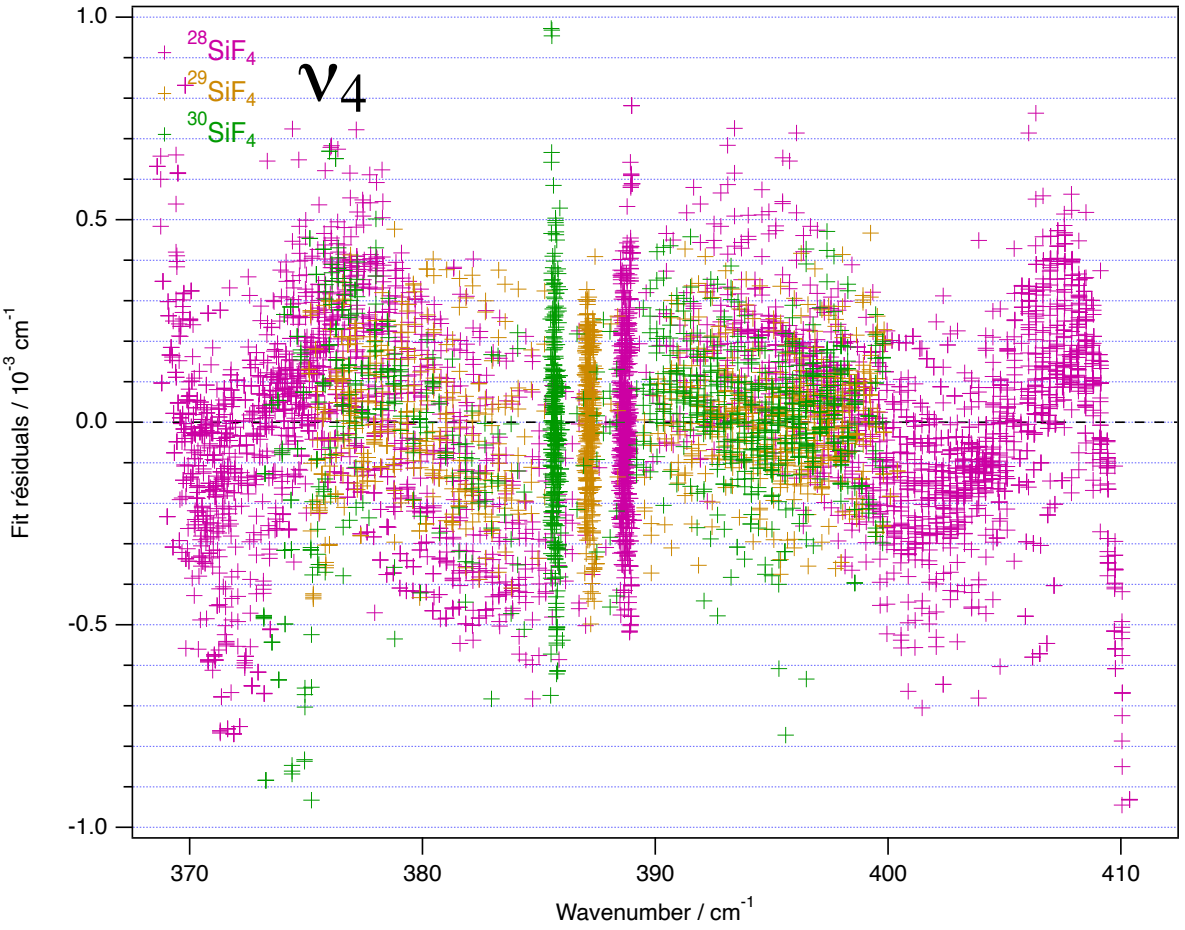

Figure 10: Observed−calculated line positions for the ν_4−GS rovibrational lines.

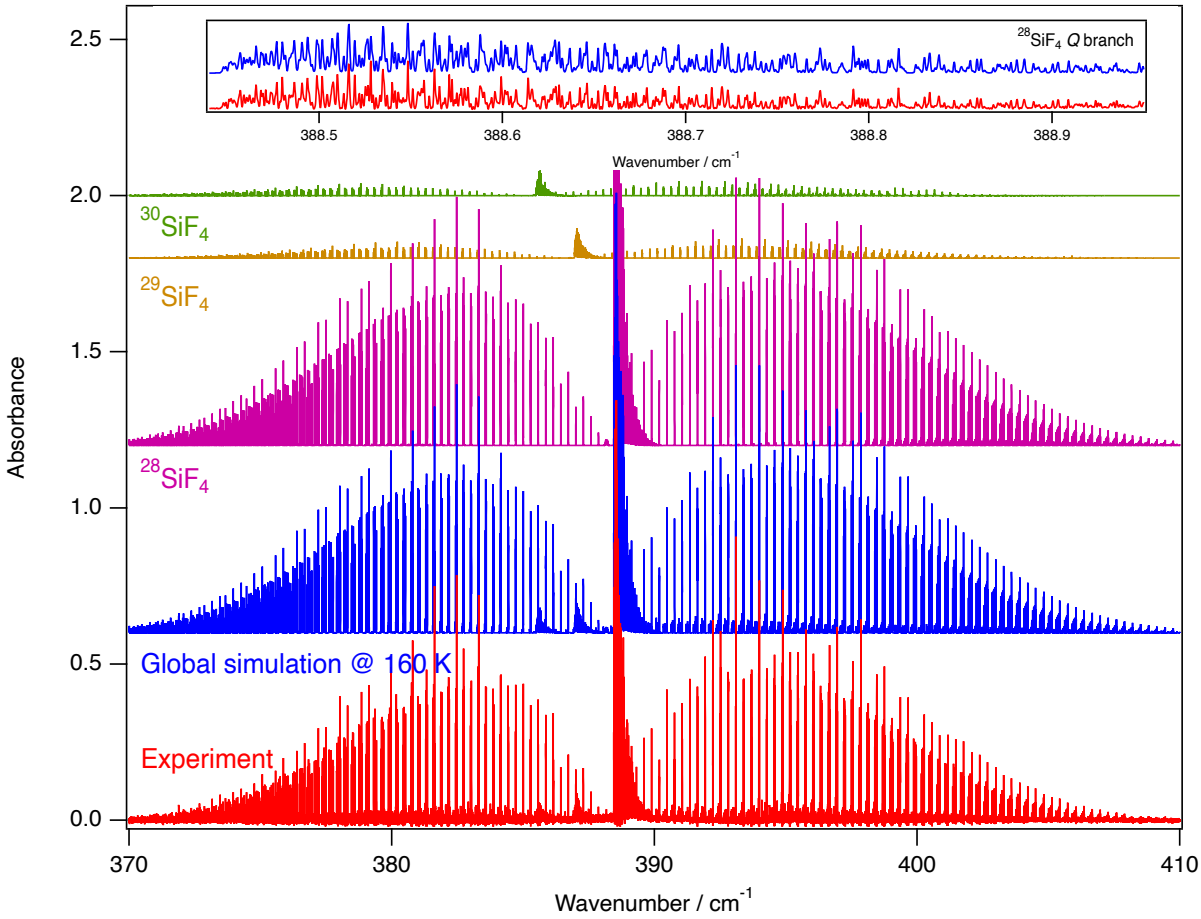

Figure 11: Overview of the ν_4 spectrum (spectrum #10), compared to the simulation for all isotopologues. The insert details a part of the Q branch region.

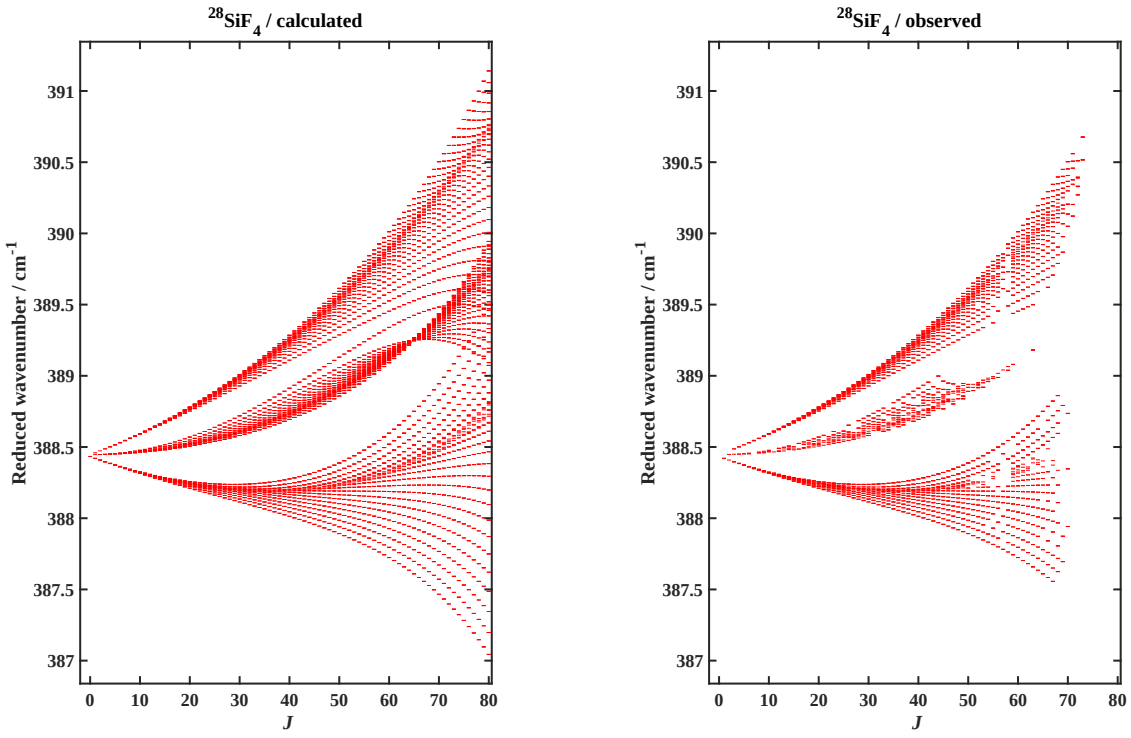

Figure 12: Observed and calculated reduced rovibrational energy levels in the $v_4 = 1$ state for $^{28}SiF_4$. Observed levels are those reached by assigned transitions.

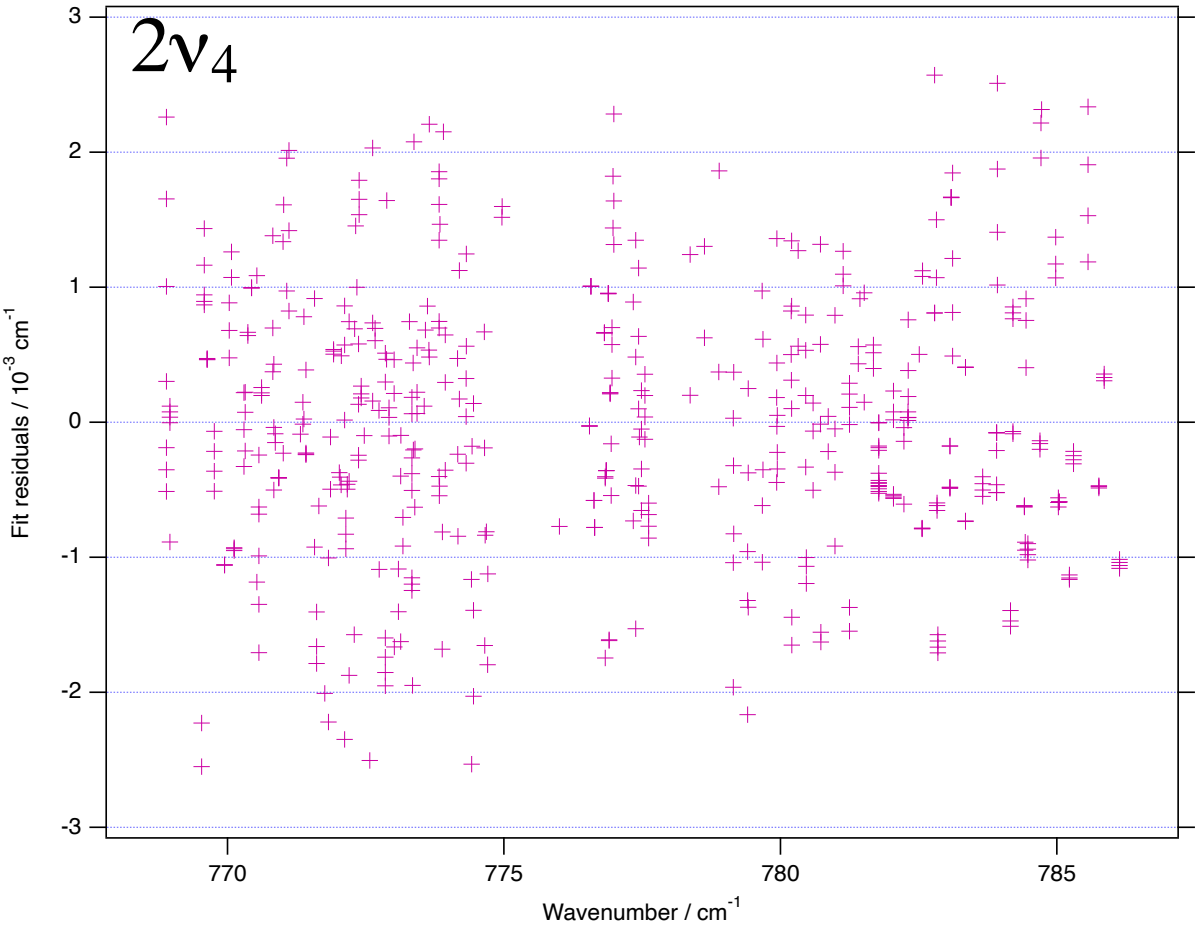

Figure 13: Observed−calculated line positions for the $2\nu_4$−GS rovibrational lines.

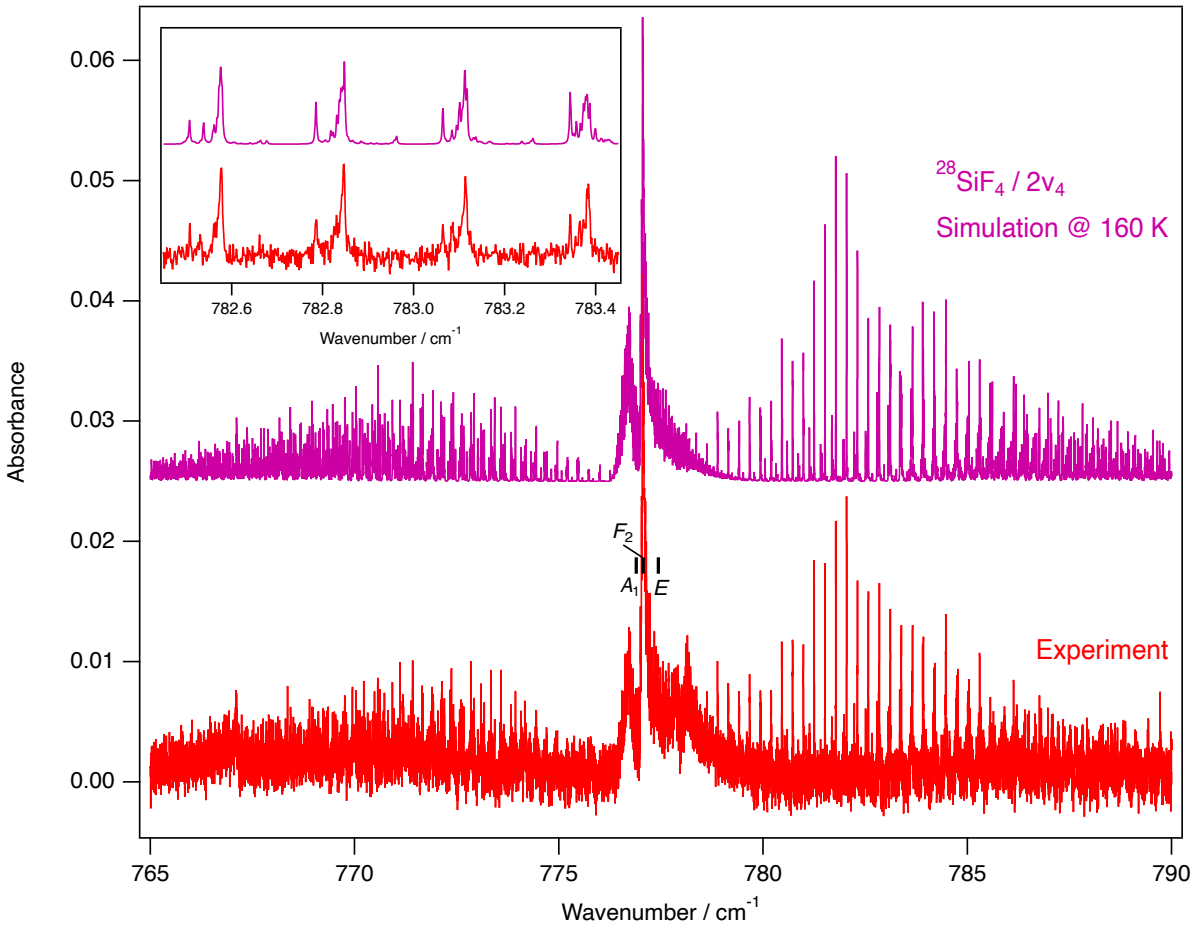

Figure 14: Overview of the $2\nu_4$ spectrum (spectrum #11), compared to the simulation for $^{28}SiF_4$. The positions of the three vibrational sublevels are indicated. The insert details a part of the R branch region.

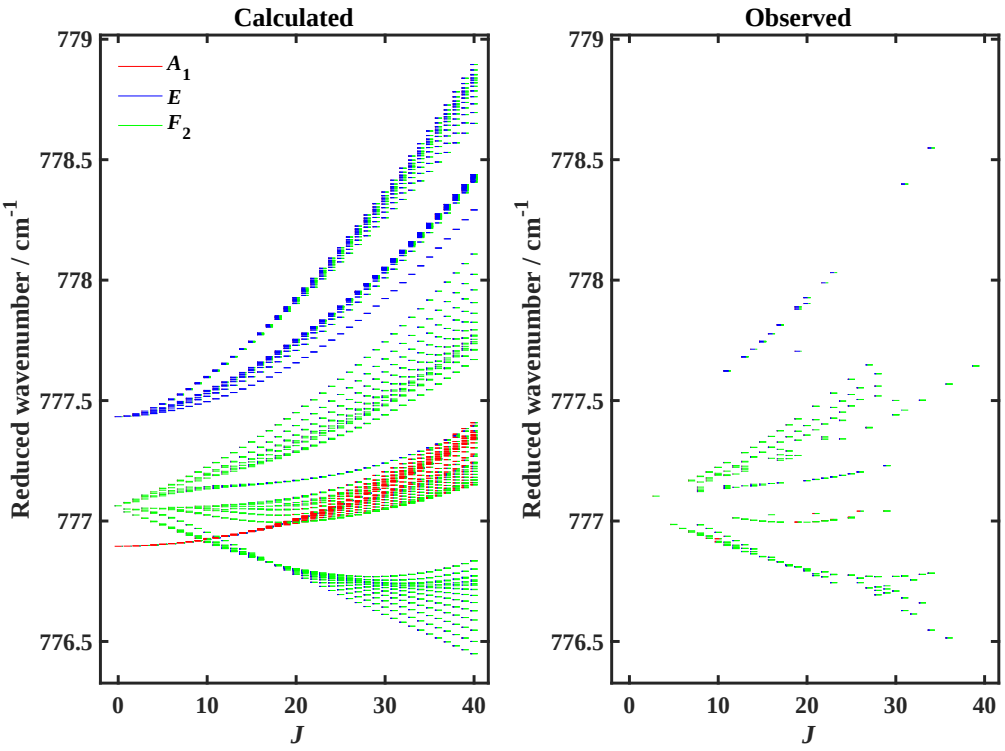

Figure 15: Observed and calculated reduced rovibrational energy levels in the $v_4 = 2$ state for $^{28}SiF_4$. Observed levels are those reached by assigned transitions. The colors illustrate the mixings between the three vibrational sublevels.

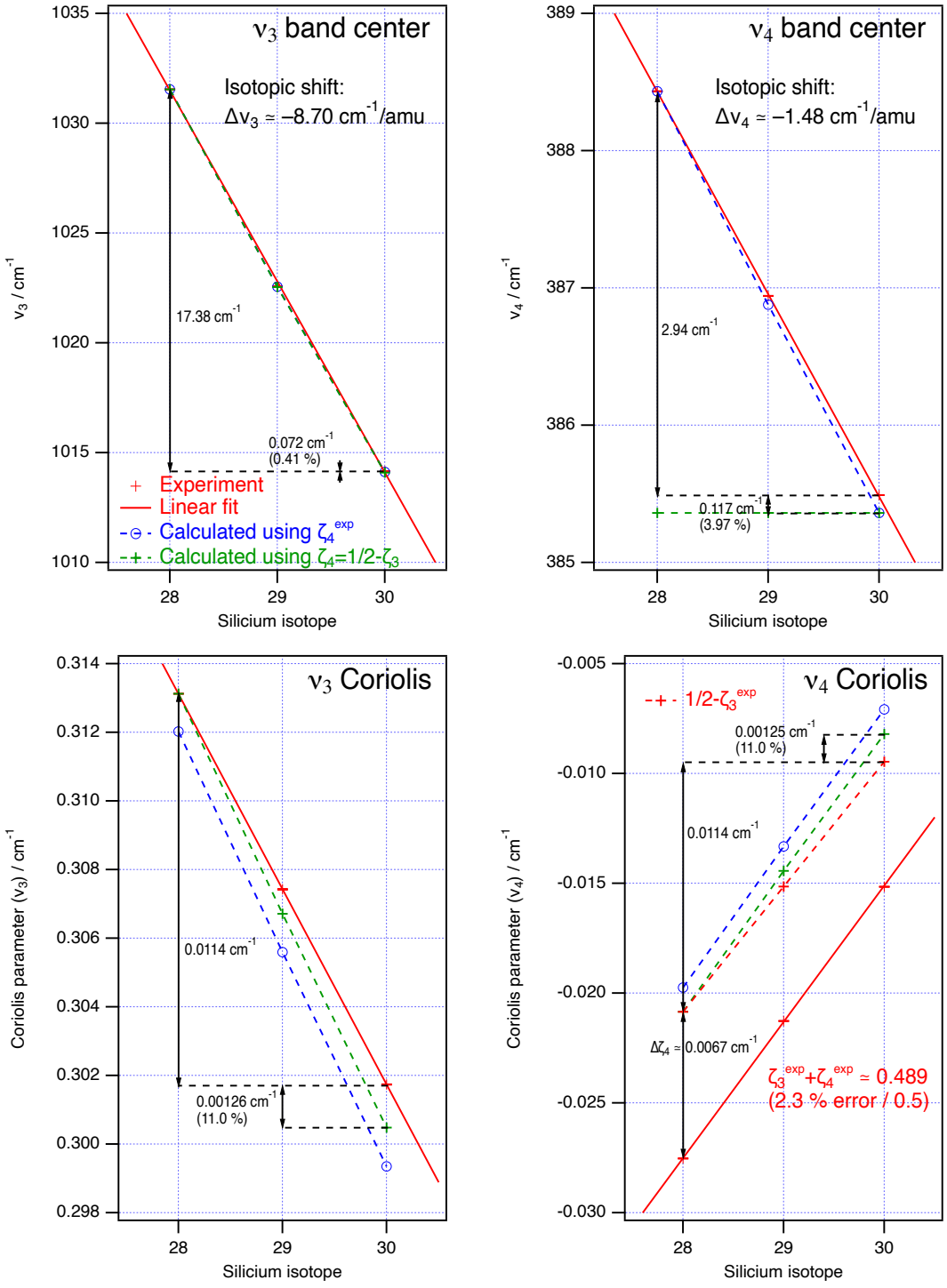

Figure 16: Isotopic dependence of the ν_3 and ν_4 band centers and Coriolis parameters for SiF_4. Calculations are performed starting with $^{28}SiF_4$ values and the resulting extrapolation error for $^{30}SiF_4$ is indicated. The calculation is done using both the experimental (in blue) and calculated (in green, through the zeta sum rule) ζ_4 value.

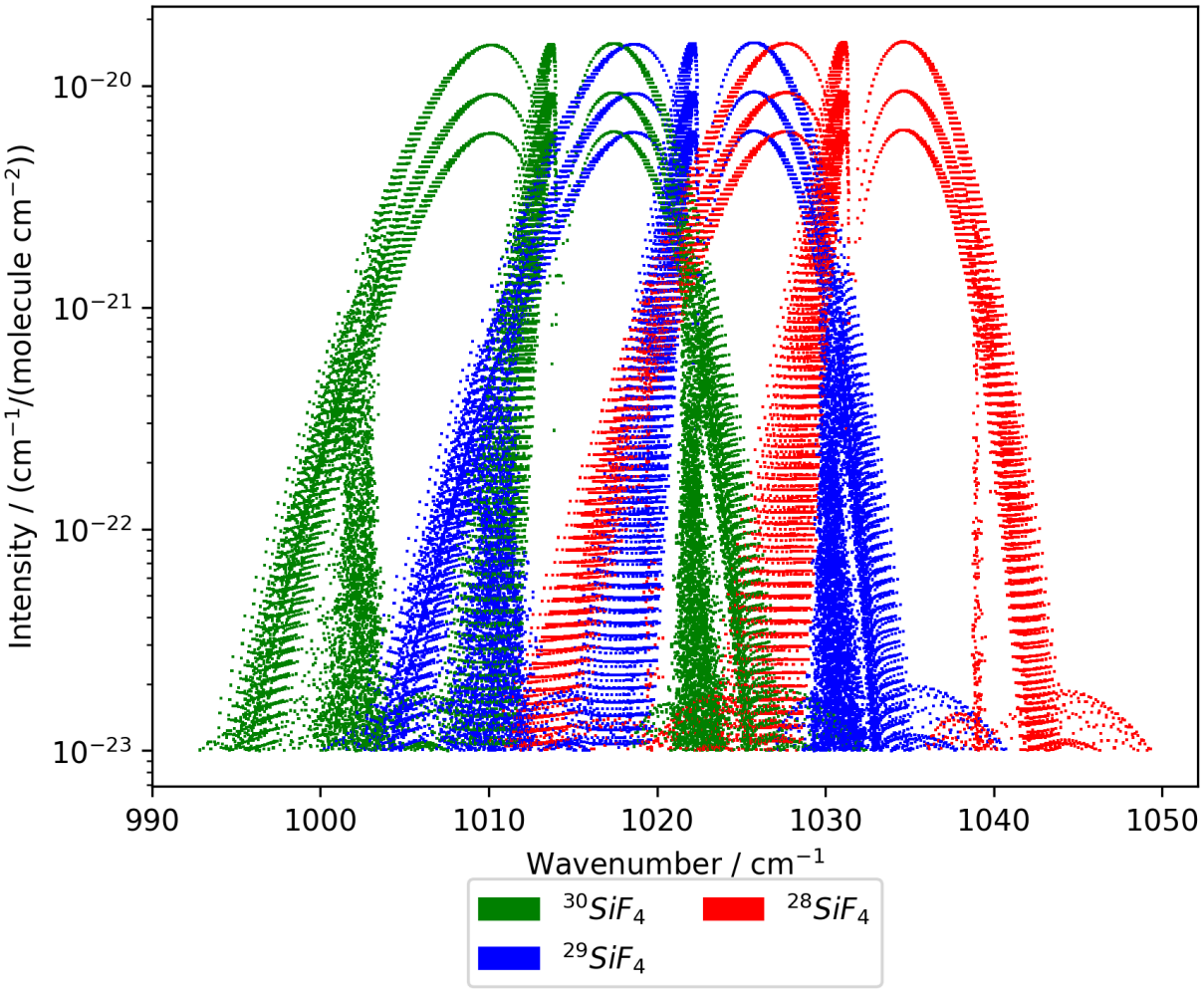

Figure 17: Extracted line by line list plotted on a graph as shown at the TFSiCaSDa web page (`https://vamdc.icb.cnrs.fr/PHP/SiF4.php`).

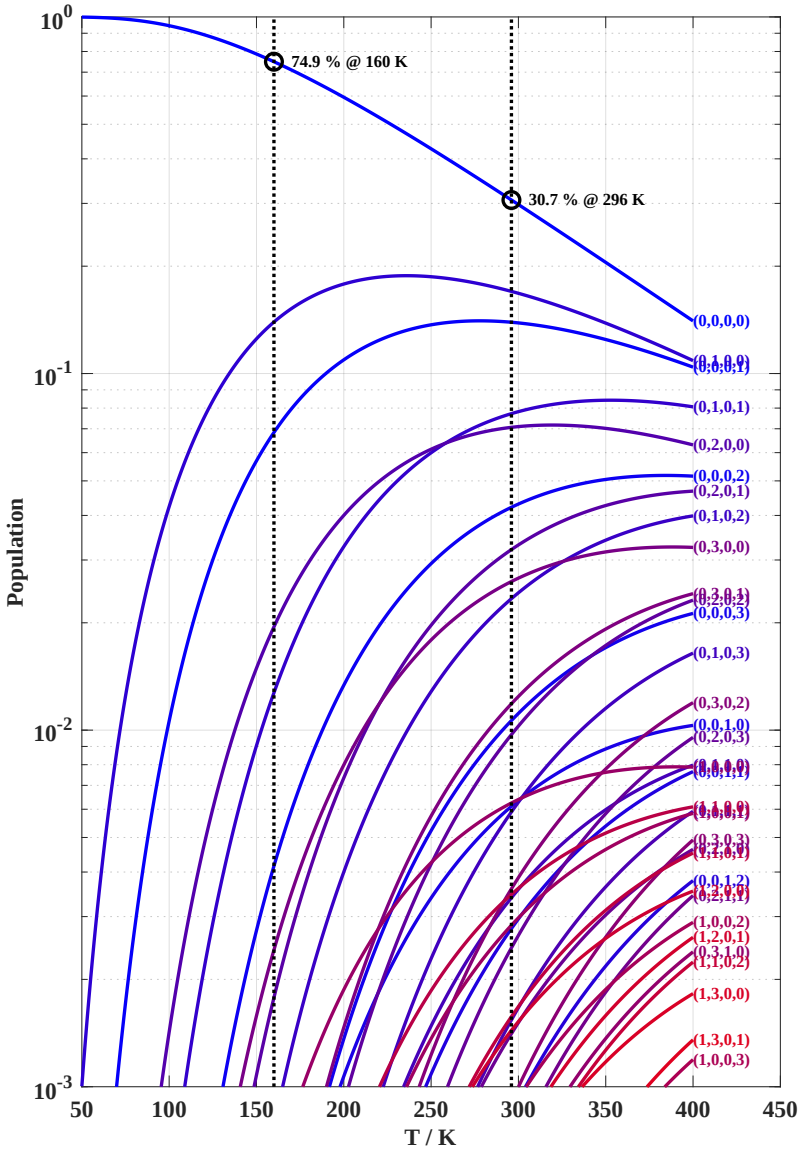

Figure 18: Population of the SiF_4 vibrational energy levels at thermodynamical equilibrium, as a function of the temperature. Vibrational levels are denoted in the form (v_1, v_2, v_3, v_4) on the right of each curve (anharmonic splittings are ignored). The value for the ground state level at room and 160 K temperature is indicated.

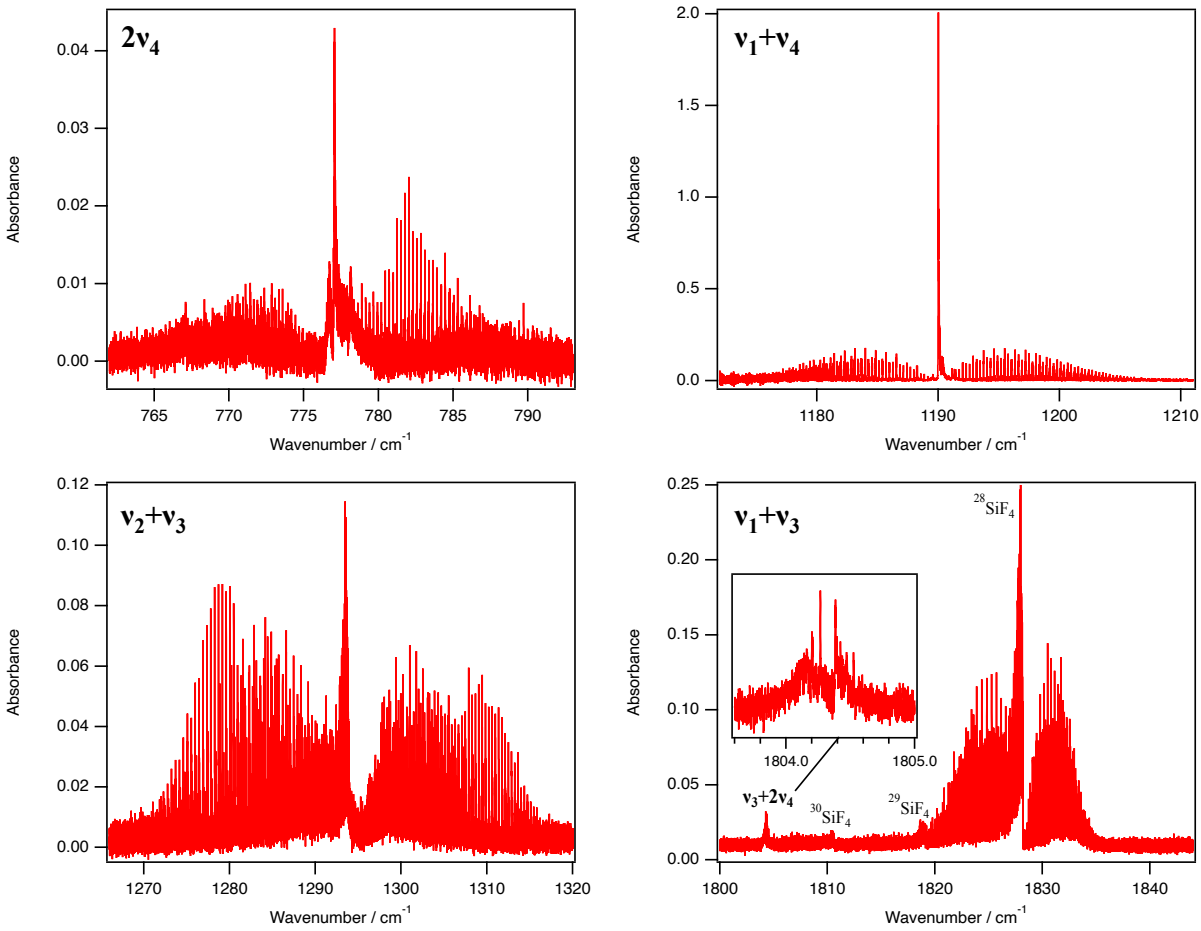

Figure 19: Experimental spectra of some overtone and combinations bands of SiF_4 (spectrum #12). The $2\nu_4$ overtone band could be analyzed in the present study. The Q branches of the $\nu_1 + \nu_3$ band of $^{29}SiF_4$ and ^{30}SiF4 are slightly visible. A weak but quite complex Q branch of the $\nu_3 + 2\nu_4$ band is visible below $\nu_1 + \nu_3$, near 1804 cm^{-1} and is expanded in the insert.

Tables

Table 1: Summary of experimental conditions adjusted for the seven spectra used in this study.

Spectrum number	Temperature / K	Pressure of SiF_4 / mb	Number of averaged scans	Resolution /cm^{-1}	Beam-splitter	Optical filter /cm^{-1}	Iris diameter /mm	Electronic filter /kHz	Fringe frequency /kHz
#1	296±1	0.44	302	0.00102	Ge/KBr	880 – 1180	1.15	10	80
#2	160±1	$\simeq$ 0.14	68	0.00102	Ge/KBr	880 – 1180	1.15	10	80
#3	162±1	1.64	40	0.00102	Ge/KBr	880 – 1180	1.15	10	80
#4	164±2	17.6	90	0.003	Ge/KBr	880 – 1180	1.15	10	80
#5	164±1	0.158 + 3.42 (N_2)	120	0.00102	Ge/KBr	880 – 1180	1.15	10	80
#6	155±5	0.095 + 3.51 (N_2)	80	0.00102	Ge/KBr	880 – 1180	1.15	10	80
#7	155±5	0.192 + 3.48 (N_2)	60	0.00102	Ge/KBr	880 – 1180	1.15	10	80
#8	155±5	0.226 + 3.42 (N_2)	80	0.00102	Ge/KBr	880 – 1180	1.15	10	80
#9	155±5	0.251 + 8.61 (N_2)	82	0.00102	Ge/KBr	880 – 1180	1.15	10	80
#10	160±2	$\simeq$ 0.25	570	0.0011	Si/Mylar	80 – 700	2	5	80
#11	160±2	1.9	140	0.0011	Si/Mylar	80 – 700	2	5	80
#12	164±1	8.56	90	0.0015	Ge/KBr	1180 – 1880	1.15	20	80

Table 2: Effective Hamiltonian parameters for the ground vibrational state, ν_3 and ν_4 fundamental bands for all three isotopoplogues. Standard deviation is indicated in parentheses, in the unit of the last two digits.

		$v_3 = 1$				$v_4 = 1$				Notation of Robiette *et al.* [42, 29]
Level	$\Omega(K, nC)$	$^{28}SiF_4$	$^{29}SiF_4$	$^{30}SiF_4$		$^{28}SiF_4$	$^{29}SiF_4$	$^{30}SiF_4$		(when available; $i = 3$ or 4)
$v = 0$	$2(0,0A_1)$	1.3778094(13)	†	†	$\times 10^{-1}$	†	†	†	$\times 10^{-1}$	B_0
	$4(0,0A_1)$	-4.218(31)	†	†	$\times 10^{-8}$	†	†	†	$\times 10^{-8}$	$-D_0$
	$4(4,0A_1)$	-3.40228(70)	†	†	$\times 10^{-9}$	†	†	†	$\times 10^{-9}$	$-\left(\sqrt{15}/4\sqrt{2}\right) D_{0t}$
	$6(0,0A_1)$	1.33(17)	†	†	$\times 10^{-12}$	†	†	†	$\times 10^{-12}$	H_0
	$6(4,0A_1)$	-2.913(26)	†	†	$\times 10^{-14}$	†	†	†	$\times 10^{-14}$	$\left(3\sqrt{5}/16\sqrt{2}\right) H_{4t}$
	$6(6,0A_1)$	1.191(59)	†	†	$\times 10^{-15}$	†	†	†	$\times 10^{-15}$	$-\left(\sqrt{231}/64\sqrt{2}\right) H_{6t}$
	$8(0,0A_1)$	2.98(15)	†	†	$\times 10^{-16}$	†	†	†	$\times 10^{-16}$	L_0
	$8(4,0A_1)$	-5.326(30)	†	†	$\times 10^{-18}$	†	†	†	$\times 10^{-18}$	$-\left(3\sqrt{15}/64\sqrt{2}\right) L_{4t}$
	$8(6,0A_1)$	5.23(23)	†	†	$\times 10^{-19}$	†	†	†	$\times 10^{-19}$	$\left(3\sqrt{77}/256\sqrt{2}\right) L_{6t}$
	$8(8,0A_1)$	1.636(86)	†	†	$\times 10^{-19}$	†	†	†	$\times 10^{-19}$	$\left(1/32\sqrt{33}\right) L_{8t}$
$v = 1$	$0(0,0A_1)$	1031.544548(63)	1022.575194(94)	1014.164535(80)		388.433387(47)	386.942121(56)	385.490187(78)		ν_i
	$1(1,0F_1)$	3.1312581(20)	3.07422(10)	3.017364(67)	$\times 10^{-1}$	-2.75276(53)	-2.12729(69)	-1.5157(13)	$\times 10^{-2}$	$3\sqrt{2}\ B\zeta_i$ (ν_i Coriolis)
	$2(0,0A_1)$	-2.9764(13)	-2.9208(30)	-2.8761(25)	$\times 10^{-4}$	1.68325(45)	1.67495(56)	1.6661(10)	$\times 10^{-4}$	$B_i - B_0$
	$2(2,0E\ )$	2.531889(74)	2.4736(46)	2.4274(26)	$\times 10^{-4}$	-1.1630(17)	-1.1713(18)	-1.1862(35)	$\times 10^{-4}$	$-(1/2)\alpha_{220} - 6\alpha_{224}$
	$2(2,0F_2)$	-9.96422(77)	-9.656(53)	-9.396(36)	$\times 10^{-5}$	5.466(19)	5.482(23)	5.499(58)	$\times 10^{-5}$	$-(3/4)\alpha_{220} + 6\alpha_{224}$
	$3(1,0F_1)$	1.1226(66)	1.037(68)	0.858(32)	$\times 10^{-7}$	-7.88(24)	-8.91(28)	-6.81(91)	$\times 10^{-8}$	$-(3(\sqrt{3})/4(\sqrt{2})F_{110}$
	$3(3,0F_1)$	-7.9(1.3)	-41.7(80)	-38.2(31)	$\times 10^{-9}$	-1.931(17)	-1.987(19)	-2.099(60)	$\times 10^{-7}$	$(3/\sqrt{5}/2)F_{134}$
	$4(0,0A_1)$	3.04(72)	6.8(2.4)	1.7(2.1)	$\times 10^{-10}$	0.0	0.0	0.0		$-(D_i - D_0)$
	$4(2,0E\ )$	-2.32(27)	-5.74(89)	-4.79(29)	$\times 10^{-9}$	0.0	0.0	0.0		$\left(\sqrt{3}/8\right) G_{220} + \left(3\sqrt{3}/2\right) G_{224}$
	$4(2,0F_2)$	2.72(28)	6.31(88)	5.68(30)	$\times 10^{-9}$	2.04(78)	2.39(56)	-3.5(3.1)	$\times 10^{-10}$	$\left(3\sqrt{3}/16\right) G_{220} - \left(3\sqrt{3}/2\right) G_{224}$
	$4(4,0A_1)$	8.69(46)	†	†	$\times 10^{-11}$	0.0	0.0	0.0		$\left(-3\sqrt{5}/4\sqrt{2}\right) (D_{4t} - D_{0t})$
	$4(4,0E\ )$	3.90(41)	9.9(1.4)	8.67(43)	$\times 10^{-9}$	5.98(96)	5.54(83)	-2.3(2.6)	$\times 10^{-10}$	$\left(-3\sqrt{7}/2\right) G_{244} + \left(\sqrt{21}/2\sqrt{22}\right) G_{246}$
	$4(4,0F_2)$	2.75(31)	7.2(1.0)	6.36(32)	$\times 10^{-9}$	4.35(70)	4.66(48)	-5.0(2.7)	$\times 10^{-10}$	$\left(-9\sqrt{7}/8\right) G_{244} - \left(\sqrt{21}/\sqrt{22}\right) G_{246}$
	$5(1,0F_1)$	0.0	0.0	0.0		7.99(48)	†	19.1(29)	$\times 10^{-12}$	
	$5(3,0F_1)$	-6.4(5.0)	-176(83)	-105(27)	$\times 10^{-13}$	-5.7(1.3)	†	-14.6(75)	$\times 10^{-12}$	
	$5(5,0F_1)$	2.28(50)	-14.7(86)	-9.7(2.8)	$\times 10^{-12}$	-8.3(1.3)	†	-19.7(73)	$\times 10^{-12}$	
	$5(5,1F_1)$	-4.29(51)	-13.4(25)	-11.01(80)	$\times 10^{-12}$	-4.68(62)	†	4.4(4.1)	$\times 10^{-12}$	
	$6(0,0A_1)$	-1.78(12)	†	0.80(34)	$\times 10^{-13}$	-6.42(45)	†	5.0(1.9)	$\times 10^{-14}$	$H_i - H_0$
	$6(2,0E\ )$	2.9(1.8)	†	†	$\times 10^{-15}$	5.26(55)	†	-6.3(2.3)	$\times 10^{-14}$	
	$6(2,0F_2)$	-2.26(29)	†	†	$\times 10^{-14}$	-5.6(1.1)	†	-22.6(82)	$\times 10^{-14}$	
	$6(4,0A_1)$	-4.84(73)	†	†	$\times 10^{-15}$	1.091(84)	†	3.62(68)	$\times 10^{-14}$	
	$6(4,0E\ )$	0.0	0.0	0.0		-8.9(5.2)	†	†	$\times 10^{-15}$	
	$6(4,0F_2)$	0.0	0.0	0.0		0.0	0.0	0.0		
	$6(6,0A_1)$	0.0	0.0	0.0		0.0	0.0	0.0		
	$6(6,0E\ )$	0.0	0.0	0.0		2.01(24)	†	9.8(2.3)	$\times 10^{-14}$	
	$6(6,0F_2)$	0.0	0.0	0.0		1.60(54)	†	8.1(4.8)	$\times 10^{-14}$	
	$6(6,1F_2)$	0.0	0.0	0.0		-6.2(1.3)	†	-39(11)	$\times 10^{-14}$	
Abund./%		92.23	4.67	3.10		92.23	4.67	3.10		
Nb. data		3728/19/182 ‡	1193	2125		4166	1330	1272		
J_{max}		80/40/40 ‡	50	66		72	52	64		
d_{RMS} *		0.219/17/40 ‡	0.269	0.270		0.261	0.164	0.228		

†Fixed to $^{28}SiF_4$ value. ‡Values for ν_3-GS, GS$-$GS and $\nu_3 - \nu_3$, respectively. *In 10^{-3} cm^{-1}, except for GS$-$GS and $\nu_3 - \nu_3$ for which it is in kHz.

Table 3: Effective dipole moment parameters for the ν_3 fundamental band of SiF_4 (using notation defined in Section 3.2), along with experimental (exp.) and calculated (calc.) integrated band intensity, compared to literature values. Standard deviation is indicated in parentheses, when available, in the unit of the last two digits.

Parameter	This work (two methods)	Burtsev *et al.* [17] Calculated	Patterson *et al.* [13] Mean on 4 lines	Fox & Person [38] Measured
$\mu^0_{\nu_3}$/Debye	0.5444(38)	0.421	0.525(28)	0.478(25)
$\mu^1_{\nu_3}$/Debye	$0.225(94) \times 10^{-3}$	—	—	—
Nb. data	83	—	4	—
$J_{\max}$	37	—	20	—
d_{RMS}/%	5.1	—	—	—
Standard deviation	0.37	—	—	—
Integrated intensity	691(27) exp.	700(30) exp.	—	—
/km.mol^{-1}	696 calc.†	690.6 calc.‡	—	—

†Integration of the simulated spectrum, see text.

‡MP2 calculation with cc-pVQZ basis set.

Table 4: Comparison of measured and calculated band intensities for some SiF_4 vibrational bands. Uncertainty is given in parentheses, in the unit of the last digit, when available.

Transition	Wavenumber /cm^{-1}	This work /km.mol^{-1}	Burtsev *et al.* [17] /km.mol^{-1}	Calculated [39] /km.mol^{-1}
$2\nu_4$	776.	0.08(1)	0.25(2)	0.056
ν_3	1031.5	691(27)	690(30)	690‡
$\nu_1 + 2\nu_2$	1064	0.10(2)	n.o.†	0
$3\nu_4$	1164	n.o.†	0.37(2)	0.55
$\nu_1 + \nu_4$	1190	1.9(3)	2.76(18)	5.52
$\nu_2 + \nu_3$	1294	2.0(3)	2.02(15)	0.0012
$\nu_3 + \nu_4$	1419	n.o..†	0.020(14)	1.4×10^{-6}
$\nu_3 + 2\nu_4$	1804	0.08(3)	0.16(1)	2.8×10^{-4}
$\nu_1 + \nu_3$	1828	2.4(3)	2.62(18)	0.54

†n.o. = not observed.

‡Normalized on Ref. [17].

Table 5: Effective Hamiltonian parameters for the $2\nu_4$ overtone band of $^{28}SiF_4$.

Level	$\Omega(K,nC)$	$\{\Gamma_v\}\{\Gamma'_v\}\Gamma$	$^{28}SiF_4$		Comments
$v_4=2$	$0(0,0A_1)$	$A_1\ A_1\ A_1$	2.84(12)	$\times10^{-2}$	A_1 sublevel
	$2(0,0A_1)$	$A_1\ A_1\ A_1$	-6.86(39)	$\times10^{-5}$	
	$2(2,0E\ )$	$A_1\ E\ E$	2.54(35)	$\times10^{-5}$	A_1-E interaction
	$2(2,0F_2)$	$A_1\ F_2\ F_2$	-1.86(16)	$\times10^{-5}$	A_1-F_2 interaction
	$3(3,0F_2)$	$A_1\ F_2\ F_2$	$0.0^\dagger$		
	$0(0,0A_1)$	$E\ E\ A_1$	5.6639(46)	$\times10^{-1}$	E sublevel
	$2(0,0A_1)$	$E\ E\ A_1$	8.93(75)	$\times10^{-5}$	
	$2(2,0E\ )$	$E\ E\ E$	6.94(71)	$\times10^{-5}$	
	$3(3,0A_2)$	$E\ E\ A_2$	$0.0^\dagger$		
	$1(1,0F_1)$	$E\ F_2\ F_1$	2.11(16)	$\times10^{-3}$	$E-F_2$ interaction
	$2(2,0F_2)$	$E\ F_2\ F_2$	-4.50(42)	$\times10^{-5}$	$E-F_2$ interaction
	$3(1,0F_1)$	$E\ F_2\ F_1$	-1.63(52)	$\times10^{-7}$	$E-F_2$ interaction
	$3(3,0F_1)$	$E\ F_2\ F_1$	$0.0^\dagger$		
	$3(3,0F_2)$	$E\ F_2\ F_2$	$0.0^\dagger$		
	$0(0,0A_1)$	$F_2\ F_2\ A_1$	1.9641(19)	$\times10^{-1}$	F_2 sublevel
	$1(1,0F_1)$	$F_2\ F_2\ F_1$	2.57(18)	$\times10^{-4}$	F_2 Coriolis
	$2(0,0A_1)$	$F_2\ F_2\ A_1$	-4.90(49)	$\times10^{-5}$	
	$2(2,0E\ )$	$F_2\ F_2\ E$	7.60(70)	$\times10^{-5}$	
	$2(2,0F_2)$	$F_2\ F_2\ F_2$	-4.97(59)	$\times10^{-5}$	
	$3(1,0F_1)$	$F_2\ F_2\ F_1$	$0.0^\dagger$		
	$3(3,0F_1)$	$F_2\ F_2\ F_1$	$0.0^\dagger$		
Nb. data			505		
J_{max}			39		
$d_{RMS}/10^{-3}cm^{-1}$			0.967		

† Fixed value.

Table 6: Experimental and calculated line positions ($\widetilde{\nu}$) and line intensities (I) for the transitions used in the intensity fit in Section 4.2. Assignments use notations explained in Section 3.3. Double primes ($''$) and primes ($'$) represent lower-state and upper-state quantum numbers, respectively. The relative errors $\Delta I_{\rm exp}$ and $\Delta I_{\rm fit}$ are defined in the Appendix.

$\widetilde{\nu}_{\rm exp}$ /cm^{-1}	$\widetilde{\nu}_{\rm calc}$	$I_{\rm exp}$ /cm^{-2}.atm^{-1} (155 K)	$I_{\rm calc}$	$\Delta I_{\rm exp}$ /%	$\Delta I_{\rm fit}$ /%	Branch	J''	C''	α''	J'	C'	α'
1031.5243	1031.5245	0.453	0.447	10%	1.3%	R	0	A_1	1	1	A_2	1
1031.6513	1031.6515	0.475	0.445	10%	6.8%	R	1	F_1	1	2	F_2	1
1032.8900	1032.8901	1.675	1.865	20%	−10.2%	R	11	F_1	2	12	F_2	2
1033.2489	1033.2489	2.037	2.086	20%	−2.4%	R	14	F_2	3	15	F_1	2
1029.1450	1029.1450	3.192	3.384	15%	−5.7%	P	17	A_2	1	16	A_1	4
1029.0081	1029.0081	2.105	2.059	10%	2.2%	P	18	F_2	3	17	F_1	11
1029.0049	1029.0049	2.083	2.059	10%	1.1%	P	18	F_1	3	17	F_2	11
1028.8673	1028.8673	3.509	3.459	10%	1.4%	P	19	A_1	1	18	A_2	4
1028.7282	1028.7282	3.305	3.468	10%	−4.7%	P	20	A_1	2	19	A_2	4
1033.7250	1033.7250	2.150	2.207	15%	−2.6%	R	18	F_2	3	19	F_1	3
1033.7224	1033.7224	2.196	2.207	15%	−0.5%	R	18	F_1	3	19	F_2	2
1033.8396	1033.8396	3.961	3.680	15%	7.6%	R	19	A_1	1	20	A_2	1
1028.5843	1028.5842	2.083	2.075	15%	0.4%	P	21	F_2	4	20	F_1	12
1028.5893	1028.5892	2.241	2.075	10%	8.0%	P	21	F_1	4	20	F_2	13
1028.4442	1028.4442	3.192	3.432	15%	−7.0%	P	22	A_2	2	21	A_1	4
1033.9553	1033.9553	3.961	3.664	15%	8.1%	R	20	A_1	2	21	A_2	1
1033.9490	1033.9523	2.150	2.198	15%	−2.2%	R	20	F_1	4	21	F_2	2
1028.3060	1028.3059	3.169	3.390	10%	−6.5%	P	23	A_2	2	22	A_1	5
1028.3097	1028.3096	2.150	2.034	15%	5.7%	P	23	F_2	4	22	F_1	14
1034.0711	1034.0711	2.196	2.178	10%	0.8%	R	21	F_1	4	22	F_2	3
1028.3117	1028.3117	1.992	2.034	15%	−2.1%	P	23	F_1	4	22	F_2	14
1034.1818	1034.1818	3.486	3.579	15%	−2.6%	R	22	A_2	2	23	A_1	1
1028.1651	1028.1650	1.924	2.000	15%	−3.8%	P	24	F_2	4	23	F_1	15
1028.1578	1028.1578	1.901	2.000	20%	−4.9%	P	24	F_1	5	23	F_2	13
1034.2978	1034.2978	3.554	3.515	15%	1.1%	R	23	A_2	2	24	A_1	1
1028.0153	1028.0153	3.010	3.263	20%	−7.7%	P	25	A_1	2	24	A_2	5
1028.0314	1028.0314	1.833	1.958	15%	−6.3%	P	25	F_2	4	24	F_1	15
1028.0339	1028.0338	1.969	1.958	15%	0.6%	P	25	F_1	4	24	F_2	16
1027.8783	1027.8782	3.078	3.181	10%	−3.2%	P	26	A_1	2	25	A_2	6
1034.4116	1034.4115	2.060	2.062	10%	−0.1%	R	24	F_2	4	25	F_1	3
1027.8836	1027.8835	2.060	1.908	20%	7.9%	P	26	F_2	5	25	F_1	15
1027.8812	1027.8812	1.879	1.908	15%	−1.6%	P	26	F_1	4	25	F_2	16
1027.7446	1027.7446	3.282	3.088	15%	6.3%	P	27	A_2	2	26	A_1	6
1034.5312	1034.5311	1.992	2.008	15%	−0.8%	R	25	F_2	4	26	F_1	3
1034.5332	1034.5331	2.105	2.008	15%	4.8%	R	25	F_1	4	26	F_2	4
1027.7354	1027.7353	1.947	1.853	10%	5.1%	P	27	F_1	5	26	F_2	16
1034.6453	1034.6452	3.192	3.246	15%	−1.7%	R	26	A_2	2	27	A_1	1
1034.6346	1034.6346	3.146	3.246	15%	−3.1%	R	26	A_1	2	27	A_2	1
1034.6389	1034.6389	1.969	1.947	20%	1.1%	R	26	F_2	5	27	F_1	3
1034.6370	1034.6370	1.924	1.947	20%	−1.2%	R	26	F_1	4	27	F_2	3
1034.7539	1034.7539	2.920	3.136	15%	−6.9%	R	27	A_2	2	28	A_1	2
1027.4449	1027.4449	2.671	2.876	20%	−7.1%	P	29	A_2	2	28	A_1	6
1027.4559	1027.4558	2.807	2.876	15%	−2.4%	P	29	A_1	2	28	A_2	6
1034.7464	1034.7463	1.856	1.882	15%	−1.4%	R	27	F_1	5	28	F_2	3
1027.3101	1027.3100	2.829	2.760	15%	2.5%	P	30	A_1	2	29	A_2	7
1034.8661	1034.8660	2.037	1.811	15%	12.5%	R	28	F_2	4	29	F_1	4
1027.3189	1027.3189	1.698	1.656	20%	2.5%	P	30	F_2	5	29	F_1	18
1034.8629	1034.8628	1.720	1.811	10%	−5.0%	R	28	F_1	5	29	F_2	3
1027.3170	1027.3169	1.811	1.656	15%	9.4%	P	30	F_1	4	29	F_2	19
1034.9745	1034.9745	2.852	2.894	15%	−1.5%	R	29	A_1	2	30	A_2	1
1034.9676	1034.9675	1.630	1.737	20%	−6.2%	R	29	F_2	5	30	F_1	3
1027.1600	1027.1599	1.607	1.583	10%	1.5%	P	31	F_2	6	30	F_1	18
1034.9696	1034.9695	1.766	1.737	20%	1.7%	R	29	F_1	6	30	F_2	3
1027.1658	1027.1658	1.562	1.583	10%	−1.3%	P	31	F_1	5	30	F_2	19
1027.0147	1027.0147	2.286	2.514	10%	−9.0%	P	32	A_2	2	31	A_1	7
1027.0058	1027.0058	2.399	2.514	20%	−4.5%	P	32	A_1	3	31	A_2	6

Continued on next page

Table 6 – *Continued from previous page*

$\widetilde{\nu}_{\mathrm{exp}}$ /cm^{-1}	$\widetilde{\nu}_{\mathrm{calc}}$	I_{exp} /cm^{-2}.atm^{-1} (155 K)	I_{calc}	ΔI_{exp} /%	ΔI_{fit} /%	Branch	J''	C''	α''	J'	C'	α'
1035.0754	1035.0753	1.698	1.659	15%	2.3%	R	30	F_2	6	31	F_1	3
1026.8702	1026.8702	2.332	2.386	10%	−2.3%	P	33	A_2	2	32	A_1	7
1035.1888	1035.1887	1.652	1.580	10%	4.6%	R	31	F_2	6	32	F_1	3
1026.8637	1026.8637	1.562	1.431	20%	9.1%	P	33	F_2	6	32	F_1	19
1026.8756	1026.8756	1.358	1.431	15%	−5.1%	P	33	F_2	5	32	F_1	20
1035.1936	1035.1935	1.630	1.580	10%	3.2%	R	31	F_1	5	32	F_2	4
1026.8782	1026.8782	1.358	1.431	15%	−5.1%	P	33	F_1	6	32	F_2	20
1035.2979	1035.2978	2.445	2.498	10%	−2.1%	R	32	A_2	2	33	A_1	1
1026.7358	1026.7357	2.286	2.257	15%	1.3%	P	34	A_1	2	33	A_2	8
1026.7156	1026.7156	1.426	1.354	10%	5.3%	P	34	F_1	6	33	F_2	20
1035.4075	1035.4074	2.354	2.362	10%	−0.3%	R	33	A_2	2	34	A_1	2
1026.5678	1026.5678	2.173	2.127	15%	2.1%	P	35	A_1	2	34	A_2	7
1026.5877	1026.5877	1.381	1.276	15%	8.2%	P	35	F_2	6	34	F_1	21
1026.5905	1026.5905	1.358	1.276	15%	6.4%	P	35	F_1	5	34	F_2	22
1026.4425	1026.4426	1.924	1.998	20%	−3.7%	P	36	A_2	2	35	A_1	8
1026.4249	1026.4249	1.992	1.998	10%	−0.3%	P	36	A_1	3	35	A_2	7
1026.4321	1026.4322	1.177	1.199	10%	−1.8%	P	36	F_2	6	35	F_1	22
1026.4157	1026.4158	1.109	1.199	20%	−7.5%	P	36	F_1	7	35	F_2	20
1026.4292	1026.4292	1.313	1.199	10%	9.5%	P	36	F_1	6	35	F_2	21
1026.2885	1026.2885	1.924	1.871	10%	2.8%	P	37	A_2	2	36	A_1	8
1035.6154	1035.6153	2.309	2.090	15%	10.5%	R	35	A_1	2	36	A_2	1
1026.2765	1026.2765	1.222	1.123	15%	8.9%	P	37	F_1	7	36	F_2	22
1035.7402	1035.7401	1.992	1.956	10%	1.8%	R	36	A_2	2	37	A_1	2
1035.7258	1035.7257	1.969	1.956	10%	0.7%	R	36	A_1	3	37	A_2	2
1035.7317	1035.7317	1.200	1.174	10%	2.2%	R	36	F_2	6	37	F_1	4
1035.7293	1035.7292	1.177	1.174	10%	0.3%	R	36	F_1	6	37	F_2	4
1035.8414	1035.8414	1.698	1.825	10%	−7.0%	R	37	A_2	2	38	A_1	2